PIONEER OUTER PLANETS ORBITER
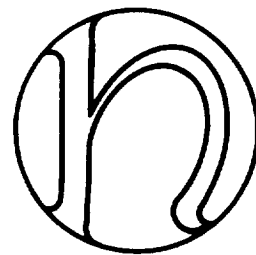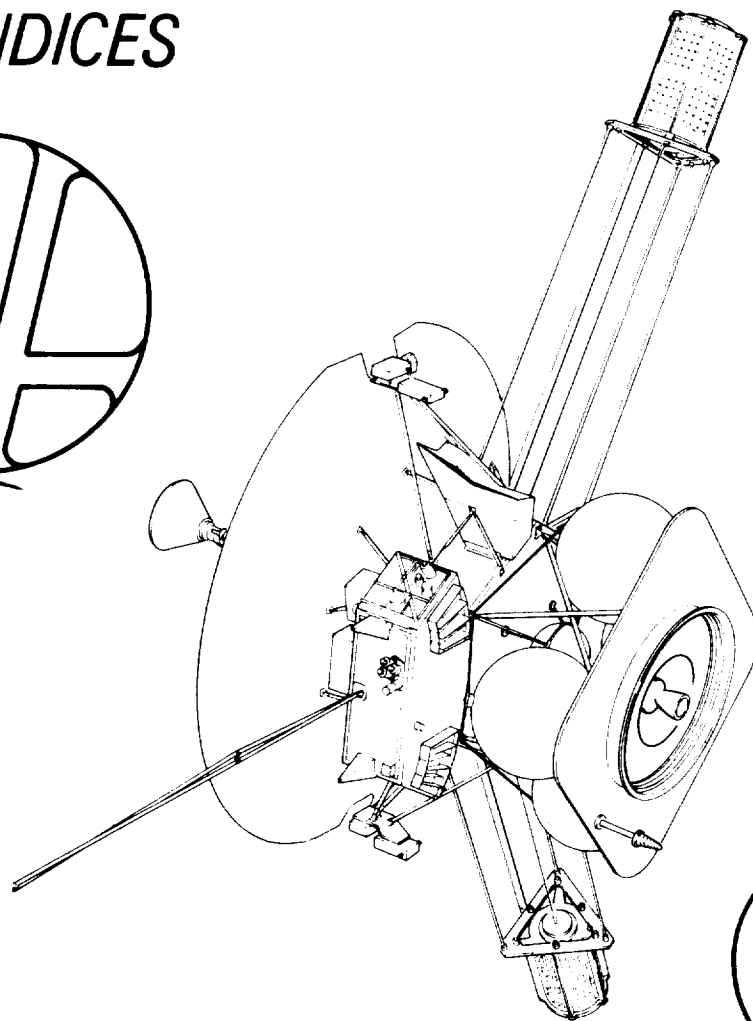
APPENDICES

NATIONAL AERONAUTICS AND SPACE ADMINISTRATION

AMES RESEARCH CENTER

MOFFETT FIELD, CALIFORNIA

10 December 1974

APPENDIX A

SCIENTIFIC INSTRUMENTS

A tentatively selected package of scientific instruments for the Jupiter and Saturn orbiter missions is described in this Appendix. As indicated in Section 3 of the main report the total payload capacity of the Pioneer Jupiter orbiter is 120 pounds, that of the Saturn orbiter 70 pounds. The sample instrument package takes up about 75 percent of the total Jupiter orbiter payload capacity. It would require a reduction by about 20 pounds to conform with that of the Saturn orbiter.

Payload interface requirements were considered in Section 2.3; the placement of the instruments was discussed in Section 3.1; other aspects of payload accommodation are described in Section 5.1.

The proposed high resolution line-scan imaging system has a far greater influence on spacecraft subsystem design and operation than any of the other payload instruments and will therefore be described in greater detail.

1. EXPERIMENT CATEGORIES

As in previous missions by Pioneer 10 and 11 and other planetary spacecraft, the Pioneer Jupiter and Saturn orbiters will carry scientific instruments for:

  a) in-situ observations of ambient phenomena during the inter-planetary cruise and in the vicinity of the target planet

  b) remote observations of planetary and satellite phenomena and features.

Sensors for in-situ observations include the particles, fields and micro-meteoroid detectors. Sensors for remote observations are the electro-optical instruments which cover the visual, infrared and ultraviolet spectral range of radiations reflected or emitted by the target body, as well as antennas that can detect radio-frequency emissions emanating from the planet or the trapped particle belts.

The in-situ observation sensors are mounted at fixed orientation relative to the spacecraft, utilizing its spinning motion as an effective means for scanning the ambient phenomena to be observed. The instantaneous roll orientation of each instrument is indexed by roll reference pulses generated by the star reference assembly, the sun sensor or an auxiliary roll reference (see Section 4.4).

The remote optical sensors can view in the desired direction only during a portion of the spin cycle. While scanning is desirable for obtaining global coverage of the target object it also imposes a constraint on the minimum required instrument sensitivity. A tradeoff between response characteristics, spin rate and resolution of observed features is required. Reduction of the spin rate may be necessary in some cases to cater to

imaging objectives (see Section 3.6). As a general requirement these sensors must be mounted on an articulated platform, so as to permit step-wise changes of the pointing angle (cone angle) as dictated by the viewing geometry (see Section 3.1). The spinning Pioneer spacecraft and three-axis stabilized spacecraft such as Mariner, have this sensor articulation requirement in common.

Earth-Based Scientific Experiments

Two types of experiments to be performed by the Pioneer Outer Planets Orbiter require no special apparatus onboard the spacecraft. These are the celestial mechanics experiments which will determine improved ephemeris data and gravitational characteristics of the target planets and satellites, and the rf-occultation experiments which will measure atmospheric characteristics. As in previous planetary missions by Pioneer and Mariner spacecraft these results will be obtained from the analysis of tracking data received at earth.

2. SELECTED INSTRUMENT COMPLEMENTS FOR JUPITER AND SATURN ORBITERS

Table A-1 lists several payload complements that have been suggested for different classes of Jupiter orbit missions by the Pioneer Outer Planets Orbiter. Scientific objectives and orbital characteristics of these mission classes are indicated in the table. The total payload weight ranges from 70 to 148 pounds. From these alternatives a representative payload complement was tentatively selected for the Jupiter orbiter, and a smaller complement for the Saturn orbiter, commensurate with payload weight capacities of the two spacecraft. These complements are listed in Table A-2. The payload instruments carried by Pioneer 10 and 11 are also listed for comparison.

3. INSTRUMENT DESCRIPTIONS

The instruments selected for the Jupiter orbiter and the phenomena to be observed will be briefly described in this section. Three of the instruments are adapted from Pioneer 10 and 11. The others (except the line-scan image system to be discussed in Section A-4) are similar to instruments flown on previous earth orbital and planetary missions or those being currently developed for the Mariner 1977 Jupiter Saturn flyby mission. Some of these descriptions also apply to instruments selected for the Saturn orbiter payload.

3.1 Vector Helium Magnetometer

The vector helium magnetometer adapted from Pioneer 10/11 will be used to measure interplanetary fields during the transit phase; to study how the solar wind and Jupiter interact; and to map the magnetic fields of Jupiter and possibly some of its satellites. The instrument is designed for measurement of field components in three dimensions.

Table A-1. Suggested Payload Complements for Four Jupiter Orbit Mission Classes

Mission	I				II				III				IV			
Objectives																
Jupiter	x				x				x				x			
Satellites (maximum number)	x (2)				x (3)								x (2)			
Atmosphere	x								x							
Magnetosphere	x								x				x			
Periapsis (R_J)	1.01				2.3				1.01				≥4			
Orbit Inclination	Minimum				Zero				High				Zero			
Instruments (weights in pounds)																
1. Jupiter and Satellites																
Visible imager	15	15	25	45	35	35	45	45	6	15	25	45	20	25	35	45
Infrared instrument	8.5	8.5	16.5	16.5	16.5	20	28	36		8.5	16.5	28	8.5	16.5	28	36
Ultraviolet instrument	6	6	6	14.5	15	15	15	20	2.5	6	15		6	7	15	20
Absolute photometer					3.5	3.5	3.5	3.5		3.5	3.5	3.5		3.5	3.5	3.5
2. Atmosphere																
Skimmer*	24	24	27	30					24	30	30	30				
3. Magnetosphere																
Magnetometer	6	6	6	6		6	6	6	6	6	6	6	6	6	6	6
Charged particle detector	6.5	10	10	10		6.5	6.5	6.5	8.5	8.5	8.5	8.5	6.5	6.5	6.5	8.5
RF receiver	4	4	6.5	6.5		4	6.5	6.5	4	6.5	6.5	6.5	4	6.5	6.5	6.5
Plasma analyzer		12	12	12				12	12	12	12	12	12	12	12	12
Plasma wave detector		3.5	3.5	3.5			3.5	3.5	3.5	3.5	3.5	3.5	3.5	3.5	3.5	3.5
Suprathermal detector				3.5					3.5	3.5	3.5	3.5	3.5	3.5	3.5	3.5
Total weight (pounds)	70	89	112.5	147.5	70	90	114	139	70	89.5	118	146.5	70	90	119.5	144.5

*Includes: mass spectrometer, retarded potential analyzer and photoelectron detector.

A-3

Table A-2. Tentatively Selected Scientific Payload Complements

Instrument	Pioneer 10/11		Jupiter Orbiter		Saturn Orbiter		Data Rate (bits/s)
	Weight (lb)	Power (W)	Weight (lb)	Power (W)	Weight (lb)	Power (W)	
Magnetospheric Particles and Fields							
Magnetometer	5.9	3.1	6.0	4.0	5.2	4.0	25
Plasma analyzer	12.0	4.5	12.0	5.0	11.5	5.0	50
Charged particle	7.2	2.4	10.0	4.0			
Geiger tube telescope	3.6	0.8	—	—	12.6	6.0	
Cosmic ray telescope	7.1	2.8	—	—			
Suprathermal particle detector	—	—	3.5	2.0	—	—	10
RF sweep receiver	—	—	6.5	3.0	—	—	250
Plasma wave detector	—	—	3.5	2.0	—	—	10
Trapped radiation detector	3.9	2.1	—	..	—	—	
Subtotal	39.7	15.7	41.5	20.0	29.3	15.0	
Planetology							
Infrared	4.4	1.2	12.0	4.0	6.0	4.0	1,000
Ultraviolet	1.5	1.0	10.0	3.0	6.0	3.0	200
Photopolarimeter	9.5	3.5	—	—	—	—	
Imaging							
Line-scan imaging system			25.0	16.0	25.0	16.0	10^6
Subtotal	15.4	5.7	47.0	23.0	37.0	23.0	
Meteoroid Detectors	11.0	2.5	—	—	3.7	1.0	
Unspecified	—	—	31.5	14.0	—	—	<12,000
Total	66.1	23.9	120.0	57.0	70.0	39.0	

Characteristics of Jupiter's interior may be inferred from the observed phenomena. The instrument may also detect interactions between Jupiter's satellites and charged particles in the Jovian magnetosphere.

The magnetometer sensor is a quantum mechanical device containing a source of circularly polarized infrared radiation, a helium absorption cell which is optically pumped by the incident IR at 1.08 microns and an infrared detector to measure the absorption of the infrared radiation by the helium cell. The helium cell is enclosed in a 4-inch diameter, tri-axial Helmholz coil system. The amount of IR absorption depends upon the strength and direction of the magnetic field at the cell and thus can be used to determine strength and direction of the magnetic field surrounding the spacecraft.

The magnetometer operates in eight ranges. The lowest range covers fields from 0.016 to 4 gamma. The highest measures fields to 140,000 gamma (1.4 gauss).

The instrument weighs six pounds and uses four watts of power. It is mounted on a boom extending 21.5 feet from the center of the spacecraft. As in Pioneer 10/11 this instrument location and careful design of a magnetically clean spacecraft will assure a low background level of spacecraft-generated magnetic fields (0.1 gamma).

3.2 Plasma Analyzer

ind.
:asure
'r
ction

It
it:
wi
phe

[t
] the
)rs
:s
its
en

ope
pla
fro
the
two
qua(
tioı
mea‹
the

u-
)r
ıd

3.3

ion

dete
envi
crui:
trap|

icles

measu
fligh
tion

'our
ry
ia-

eight
isoto
tary
outer

f
)

intens
detect
measur
reach
foil o
The re

The Pioneer 10/11 trapped-radiation detectors determine the nature of particles trapped by Jupiter, i.e., particle species, angular distribution and intensities. The instruments measure a broad range of energies: electrons from 0.01 to 100 MeV, and protons from 0.15 to 350 MeV.

Five detectors cover the anticipated energy ranges. An unfocused Cerenkov counter counts electrons and protons with velocities greater than three-fourths the speed of light. It can detect electrons with energy above 1 MeV and protons above 450 MeV. Another detector measures electrons above 100, 200 and 400 keV.

An omnidirectional counter (a solid-state diode) discriminates between minimum ionizing particles at 400 keV and high-energy protons at 1.8 MeV.

Twin DC scintillation detectors measure the energy flux of low-energy particles. Their thresholds are 10 keV for electrons and 150 keV for protons.

3.4 Suprathermal Particle Detector

This detector is similar to the low-energy proton and electron differential energy analyzer (LEPEDEA) previously flown on OGO 3, 4 and 5, IMP 4 and Injun 5 satellites, but with increased sensitivity, dynamic range and lifetime. Its function will be to survey the differential energy spectrum of protons and electrons in the interplanetary medium and the Jovian magnetosphere.

The instrumentation employs a pair of cylindrical-plate electrostatic analyzers and continuous-channel electron multipliers. With its extended energy range and low intensity threshold it will complement the measurements performed by the plasma analyzer. Measurements will be made in 16 adjacent energy bands between 100 eV and 75 keV.

3.5 RF-Emission Detector

This experiment is similar to one currently under development for the Mariner 1977 Jupiter Saturn mission. It consists of a sweep frequency radio receiver operating between 20 kHz and 40 MHz. The signals will be received by a pair of orthogonal monopole antennas with a 40-foot tip-to-tip separation. Study of the radio emission signals from Jupiter over this range of frequencies will yield data concerning the physics of magnetospheric plasma resonances and thermal radio emissions from this planetary region.

3.6 Plasma Wave Detector

The plasma wave instrument, a device similar to one flown on Explorer 47, will provide data to answer fundamental questions on the origin and dynamics of Jupiter's magnetosphere, and the properties of the distant interplanetary (and perhaps interstellar) medium. Basic planetary dynamic processes are known to be associated with wave-particle interactions for instance, solar wind particle heating at the bow shock,

diffusion effects that allow magnetosheath plasma to populate the magnetospheres, various energization phenomena that convert thermal plasma of solar wind origin into trapped radiation, and precipitation mechanisms. Wave measurements at Jupiter will enhance understanding of the key processes known to be involved in the decameter bursts.

Local diagnostic information (such as plasma densities, magnetic field strengths, and ion composition) will be obtained from wave observations. The instrument will also search for lightning whistler evidence of atmospheric electrical discharges. A 32-channel spectrum analyzer (based on an existing IMP-6 instrument) will give continuous coverage of electric fields in the 10 Hz to 200 kHz range with high time-resolution. A modified OGO 6 search coil will be used with this analyzer for magnetic field measurements up to 10 kHz. Samples of audio frequency (10 to 300 Hz) E or B waveforms will be recorded periodically for transmission to earth at intervals determined by available bit rates.

3.7 Infrared Radiometer

Infrared radiometry will be used to obtain thermal characteristics of the Jovian atmosphere, including data on the vertical temperature profile and its gross chemical composition. The instrument will be used to determine the global and local energy balance and the net thermal energy output of Jupiter, one of the most important questions about the planet. By comparing the thermal map of the planet with visual images information to explain the origin of the visible features of the Jovian disk may be obtained. Observation of the day and night hemispheres and especially the terminator regions will yield data on local thermal anomalies. Thermal properties of Jovian satellites and their atmospheres will also be objects of observation.

The infrared radiometer flown on Pioneer 10 and 11, operating in the 14-25 micron and 29-56 micron wavelength ranges, is a possible candidate, although an instrument with greater sensitivity, resolution and extended spectral range would be preferable in the orbiter application. The instrument under development for the Mariner Jupiter Saturn spacecraft combines the capabilities of the Mariner 9 Mars Orbiter infrared radiometer and interferometer spectrometer instruments and as such would greatly exceed the 12-pound IR radiometer weight allocation of the Pioneer orbiter.

3.8 Ultraviolet Photometer

An ultraviolet photometer similar to that flown on Pioneer 10/11 may be carried by the orbiter. This instrument will be used in the orbital mission phase to identify constituents of the planetary atmosphere, to determine in particular the hydrogen-to-helium ratio, to take the temperature in the outer layers of that atmosphere and to detect auroral phenomena. During the interplanetary cruise phase the UV instrument will be used to detect the amount of neutral hydrogen in the surrounding medium, possibly also neutral helium, and the interaction of

these gases with charged particles. It will be used in attempting to detect the inner boundary of the transition zone at which the solar wind is beginning to subside.

The sensor is a two-channel photometer designed to observe the resonance emissions from atomic hydrogen at 1216 Angstrom and helium at 584 Angstrom. It uses a lithium fluoride filter and photocathodes to isolate these emission features.

Other UV observation instruments with a greater range of spectral sensitivity are also being considered, such as the UV spectrometer flown by Mariner 9 and 10.

4. CHARACTERISTICS OF THE IMAGE SYSTEM

4.1 Imaging by a Line-Scan System

The proposed imaging system consists of a linear array of a large number of solid-state photo detectors which are swept in push-broom fashion across the visual scene being observed. The line elements describe concentric circles around the spin axis, the radii of these circles being determined by the cone angle at which the optical axis of the instrument is pointed. The sweep rate varies with the sine of the cone angle. Viewing of objects at cone angles near 180 degrees is to be avoided because of the deterioration of the imaging process. Cone angles of less than 40 degrees are excluded because of field-of-view obscuration by the high-gain antenna dish.

The preference for a line-scan image system in this application is based on the following considerations:

- A point scan image system such as the imaging photo-polarimeter used on Pioneer 10 and 11 requires more complex data processing in composing images from successive scans, particularly during rapid changes of the scene close to the planet.

- Conventional image forming (vidicon) TV systems are penalized by the 5 rpm Pioneer spin rate without further state-of-technology advances. The short exposure times necessary to avoid smear would require optics of increased size.

- The solid-state line scan photodetector, developed originally for near-earth applications, is compatible with the spinning Pioneer spacecraft, offers high geometric accuracy, long life, compact design and has a low power requirement.

A recent laboratory demonstration study of a line-scan image system conducted by TRW Systems under NASA/Ames Research Center study contract verified its applicability to Pioneer outer planet orbiter and flyby missions.*

The image system is limited in resolution in the direction normal to the sensor array, i.e., the spin scan direction, by the required exposure time of each detector cell. The present state of technology requires at least 0.1 msec, which for a 5 rpm spin rate translates into about 0.05 milliradian of image smear. Resolution along the sensor array is determined geometrically by the field of view and the number of cells. The influence of other optical system characteristics must also be taken into account in a detailed performance analysis.

4.2 Description of the Solid-State Photodetector Array

The linear sensor array (LSA) shown in Figure A-1 consists of 195 phototransistors, fabricated by triple diffusion in silicon on a single chip. The array consists of two rows of phototransistors containing 97 and 98 elements, respectively. This configuration provides sufficient spacing between adjacent elements along the array to prevent crosstalk due to penetration of the incident radiation into the base material. The size of the photosensitive area of each phototransistor is 0.7×10^{-3} by 0.9×10^{-3} inches, and the pitch spacing determines the limiting spatial resolution of the array.

In addition to the 195 phototransistor elements, the semiconductor chip contains an equal number of individual amplifiers, a shift register and multiplexer. The multiplexer is used to commutate the outputs of the 195 preamplifiers onto five signal leads, each containing the serial output of 39 preamplifiers. These five signal leads are hard-wired to a second chip, containing five signal conditioning electronics (SCE) amplifiers, that further amplify the five serial signals prior to digital processing of the signals.

The equivalent circuit of one phototransistor and preamplifier element of the semiconductor chip and a typical operating cycle of the element are illustrated in Figure A-2. A bias voltage initially applied to the phototransistor through terminal V_{CC} charges the base-collector capacitance to a specified value. Light incident on the junction generates hole-electron pairs that discharge the initial bias in proportion to the amount of energy absorbed during the exposure. The voltage change of the base-collector capacitance is amplified by the preamplifier.

The 195 signals from the phototransistors are commutated in five groups of 39. Readout is accomplished by closing of the readout switches (S3), in sequence. This switching is actually accomplished by individual transistors under control of a shift register. The readout, or sampling, of the output of each preamplifier is accomplished in 2 μsec, thus 78 μsec
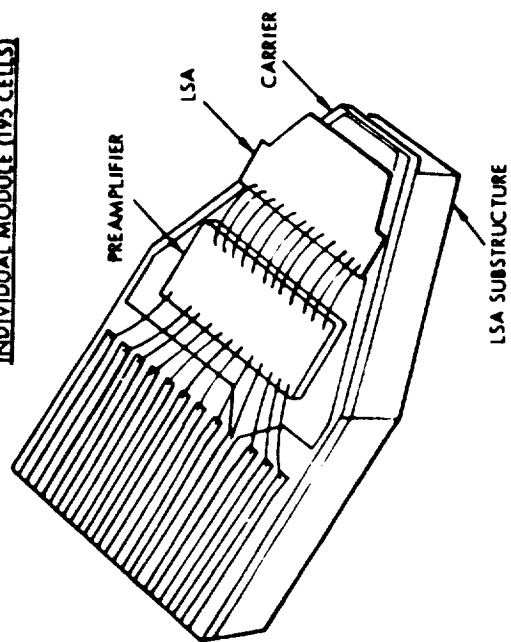
---

*"Feasibility Test of a Solid State Spin-Scan Photo-Imaging System," 23671-6001-TU-00, TRW Systems Group, 14 December 1973.

Figure A-1. Solid State Photodetector Array
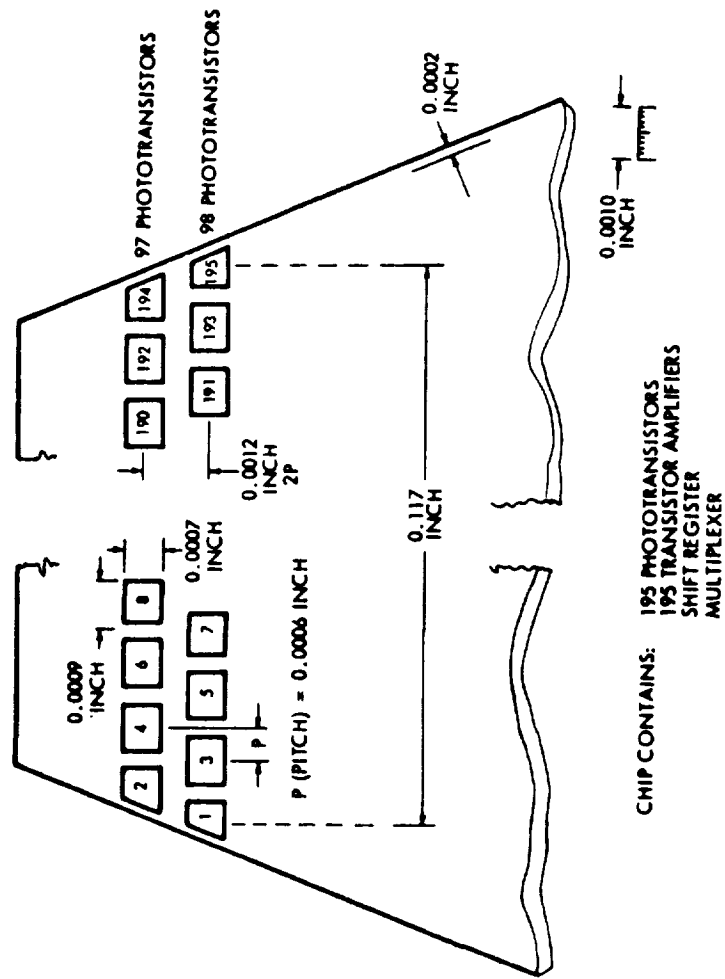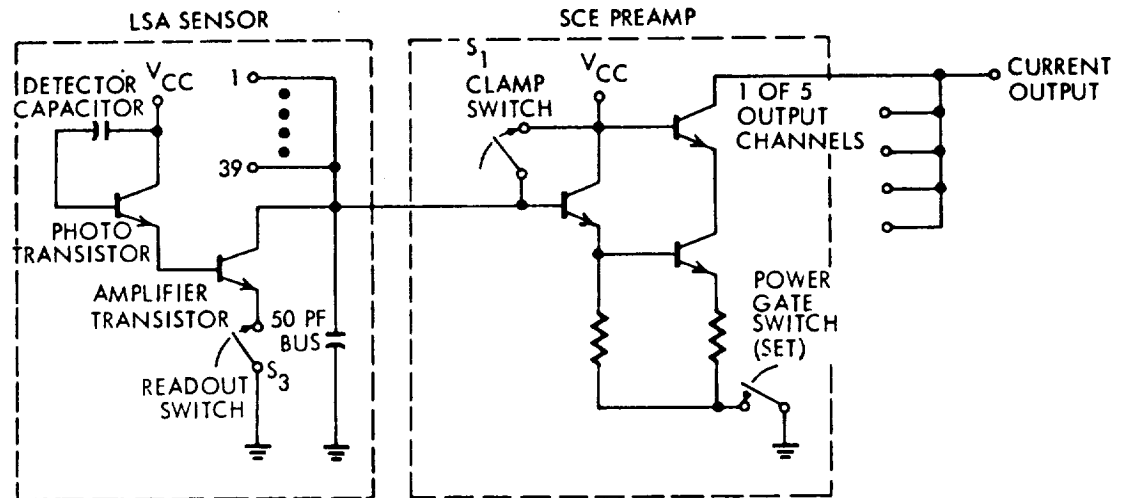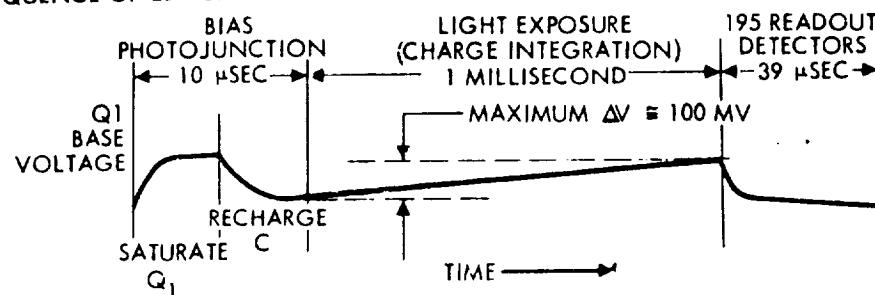
Figure A-2. Phototransistor Circuit and Operating Cycle

are required for serial sampling of each group of 39. After this samp-
ling, the photojunctions of the phototransistors are again biased, and
the cycle is repeated.

The SCE preamplifier provides two stages of gain. Five parallel
groups are contained on a single chip to amplify the five multiplexed
signals. The clamp switch, S1, is used to reset the signal to a refer-
ence level between each of the 39 serial samples from the photo sensor.
The power gate switch is used only to apply power to the SCE preampli-
fier to initiate operation.

4.3   Representative Image System Design and Performance Characteristics

The optical design and system characteristics of a representative
image system are summarized in Table A-1. For this configuration a
linear array of 390 phototransistor cells on two photodetectors was
assumed. The number of data bits per frame is 0.913×10^6 bits.

Table A-1. Representative Imaging System Characteristics

SENSOR	LINEAR ARRAY OF 390 SILICON PHOTOTRANSISTORS
OPTICAL SYSTEM	CASSEGRAIN, 4.7-IN. FOCAL LENGTH, f/1.2
INSTANTANEOUS FIELD OF VIEW	0.150 X 50 MILLIRADIANS
ANGULAR SIZE OF IMAGE	50 X 50 MILLIRADIANS (3 X 3 DEG)
SCAN PATTERN	390 TV LINES
LINE EXPOSURE TIME	0.127 MILLISECONDS (S/C ω = 5 RPM) 0.550 MILLISECONDS (S/C ω = 1 RPM)
FRAME SCAN TIME	0.495 SECONDS (S/C ω = 5 RPM) 2.14 SECONDS (S/C ω = 1 RPM)
DYNAMIC RANGE OF SENSOR	1000/1
DATA SAMPLES/TV LINE	390
ENCODING LEVEL	6 BITS/SAMPLE
DATA BITS/FRAME	0.913×10^6 BITS
WEIGHT	
OPTIC, ARRAY, PREAMPLIFIERS, MULTIPLEXER	6 LB
SIGNAL PROCESSING ELECTRONICS	5 LB
MIRROR AND POINTING MECHANISM	6 LB
POWER	
ARRAY, PREAMPLIFIERS, MULTIPLEXER AND ELECTRONICS	5 W
A/D CONVERTERS (5)	8 W
MIRROR POINTING CONTROL SYSTEM	5 W
VOLUME	
OPTIC AND ARRAY	0.15 FT^3
SIGNAL PROCESSING ELECTRONICS	0.12 FT^3
MIRROR AND POINTING MECHANISM (SWEPT VOLUME)	0.4 FT^3

Figure A-3 shows the performance of the proposed line-scan image system under conditions representative of operation at Jupiter, at 5 rpm spin rate in the broadband imaging mode. The performance is expressed in terms of signal-to-noise current and power ratios as function of spatial frequency at the image plane. The performance varies with the modulation contrast of the scene as shown parametrically for values from 5 to 100 percent contrast. The signal-to-noise ratio drops with increasing spatial frequency and decreasing scene contrast. At a spatial frequency of 32.8 line pairs per mm for the given focal length and cell array size a sharp degradation of imaging capability occurs due to coincidence of image feature and photocell spacing. In the performance graphs this singularity is indicated as resolution limit.

The data show that images with very satisfactory minimum signal-to-noise ratios (ranging from 8 to 20) are obtainable by this system even at low values of the modulation contrast. At Saturn the signal-to-noise ratio is 2 to 3 times lower than at Jupiter for a given modulation contrast. This would require a reduction of the spin rate to 2 rpm in order to increase the exposure time of the photodetectors. However, improved photodetectors currently being developed have a sensitivity
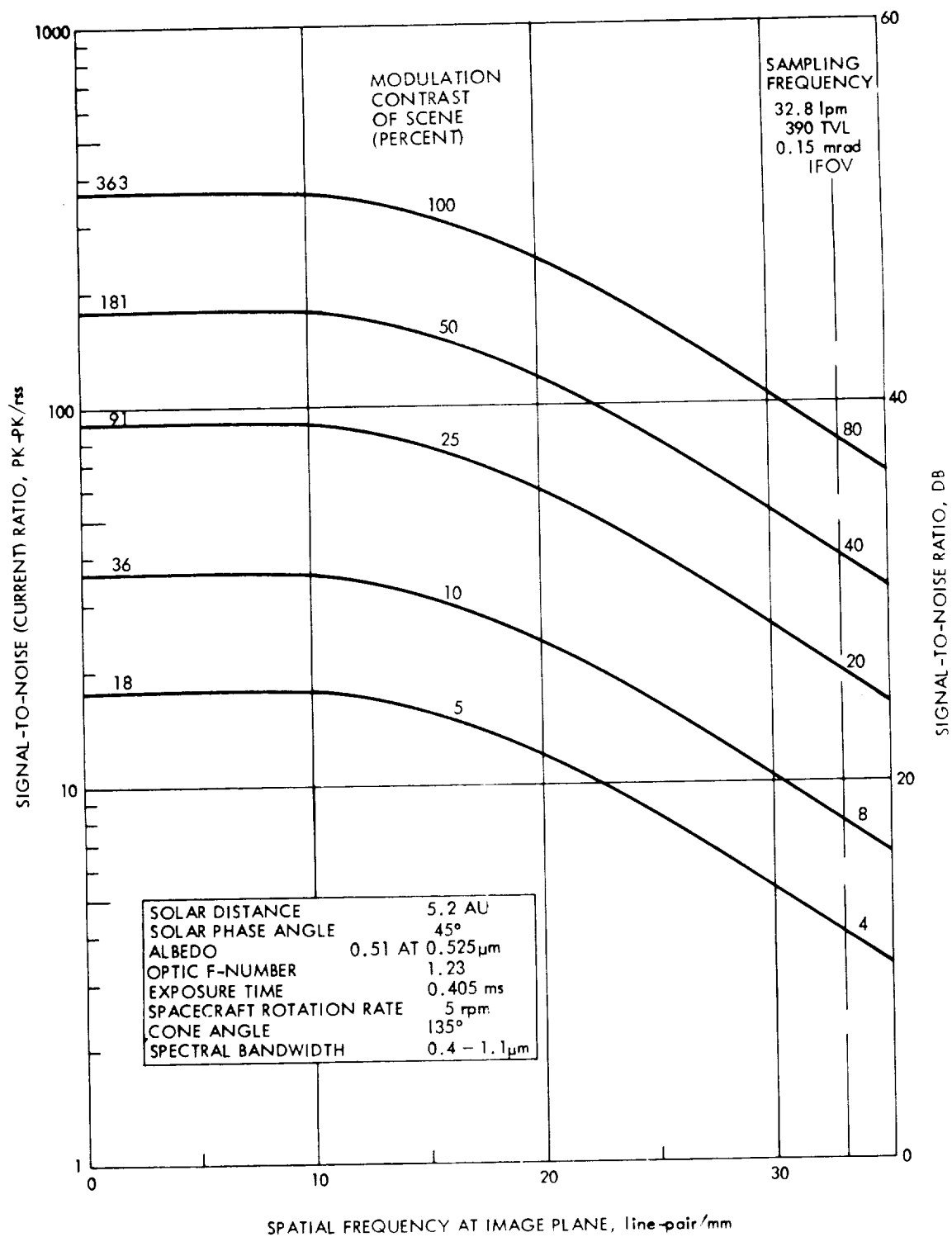
Figure A-3. Photo-Imaging System Performance
at Jupiter (Broadband Mode)

three to six times greater than phototransistors and would permit using the camera at spin rates of 5 rpm even at Saturn, with signal-to-noise ratios exceeding 10, in the broadband as well as the narrowband observation modes, if the scene modulation contrast is at least 10 percent.

4.4 Results of Laboratory Test of Line-Scan Camera

The laboratory simulation test of the line scan camera (see reference) by TRW yielded results shown in Figures A-4 and A-5 for simulated visual scenes of a planet with heavy cloud cover and for a planetary satellite without atmosphere showing features such as earth's moon. The scene brightness was adjusted to correspond to the actual scene at Jupiter's distance from the sun and at the albedo of the planet and one of its satellites (Europa). The spin motion of the spacecraft was simulated by a linear scan motion of the image system via a rotating mirror at a rate corresponding to 5 rpm. As noted in the image specimens the resolution, clarity and contrast of the scenes is well preserved by the line-scan camera.

4.5 Performance Nomograph

For a preliminary assessment of performance parameters and trade-offs the nomograph shown in Figures A-6 and A-7 is useful. The left half of the chart gives the geometrical resolution (lower left) and the image smear effect due to spin rate (upper left) as functions of focal length and exposure time, respectively. The lower right hand quadrant shows the influence of optical parameters (aperture and f-number), the upper right hand quadrant shows the influence of exposure time and f-number on the signal-to-noise ratio of the photodetector output for Jupiter and Saturn imaging. The legend indicates equivalent S/N values for broadband and multispectral operation of the camera system. The two charts represent performance characteristics of the photo-transistor (Figure A-6) and photodiode chips (Figure A-7) developed by TRW Systems. A more detailed discussion of the performance characteristics reflected in the upper right quadrants of Figures A-6 and A-7 may be found in the referenced report. The example illustrated in Figure A-6 gives the following results: assuming a resolution of 0.15 mrad (with equal optical resolution and image smear) the 390-cell phototransistor used in a camera of 10 cm focal length and 1.3 f-number gives a S/N ratio of 10 at Saturn, and 30 to 40 at Jupiter, if the spin rate is 5 rpm and the exposure time, accordingly, ~0.3 msec. A lower spin rate of 2 rpm (0.73 msec exposure time) increases the S/N ratio by a factor of 2.5.

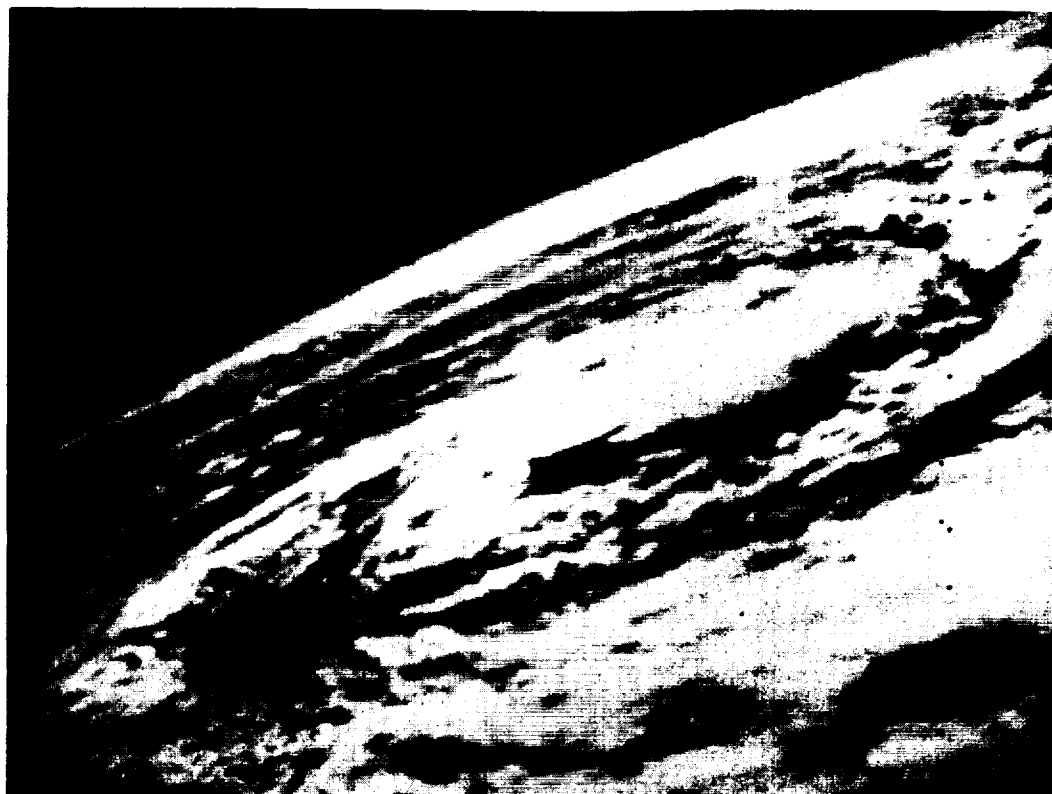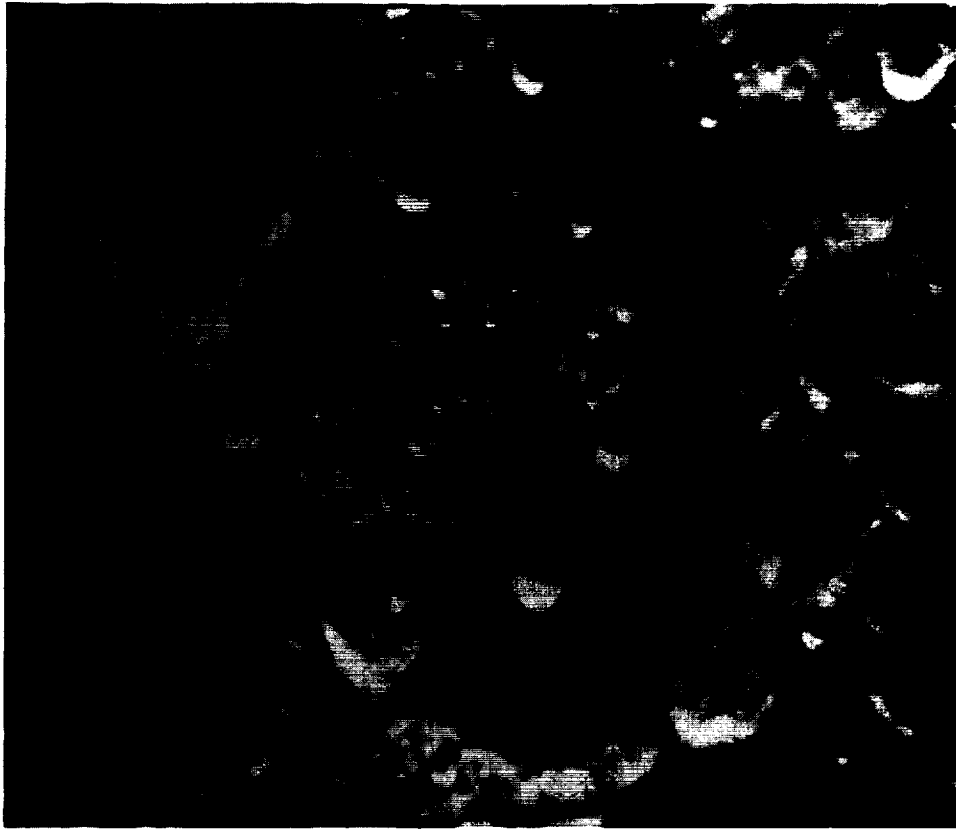(a) Scene Seen by Camera
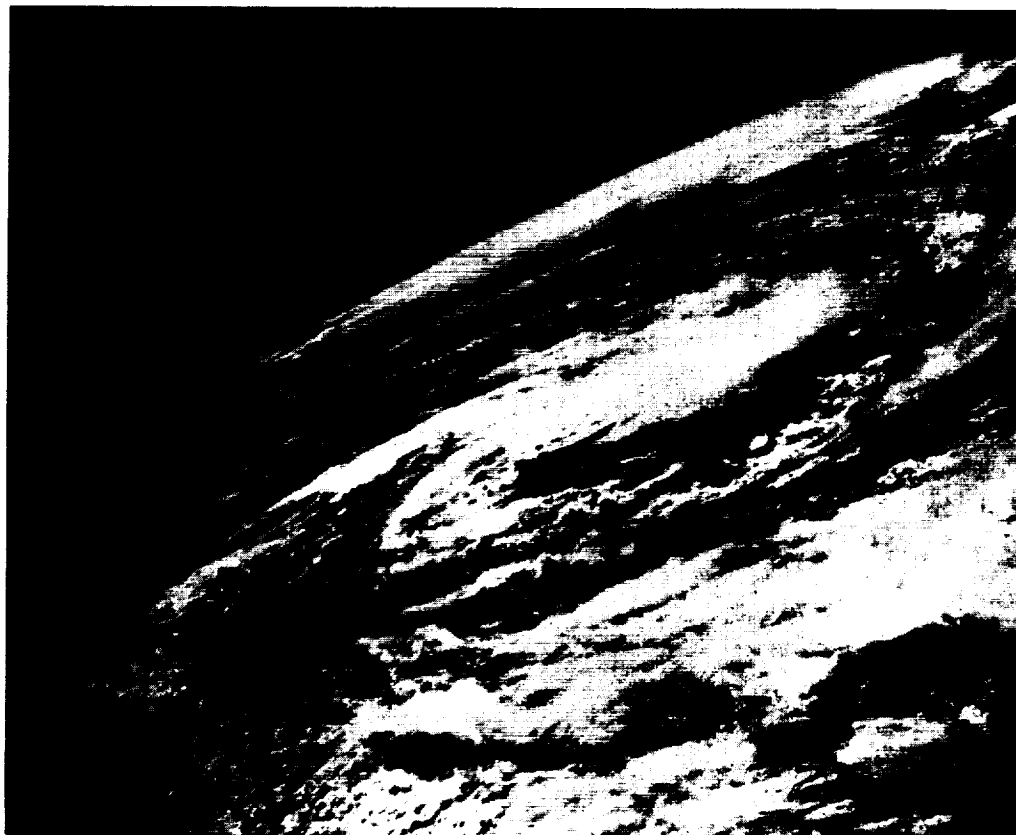
(b) Image Produced by Camera

Figure A-4. Simulated Imagery of Jupiter from Close Range

(a) Scene Seen by Camera

(b) Image Produced by Camera

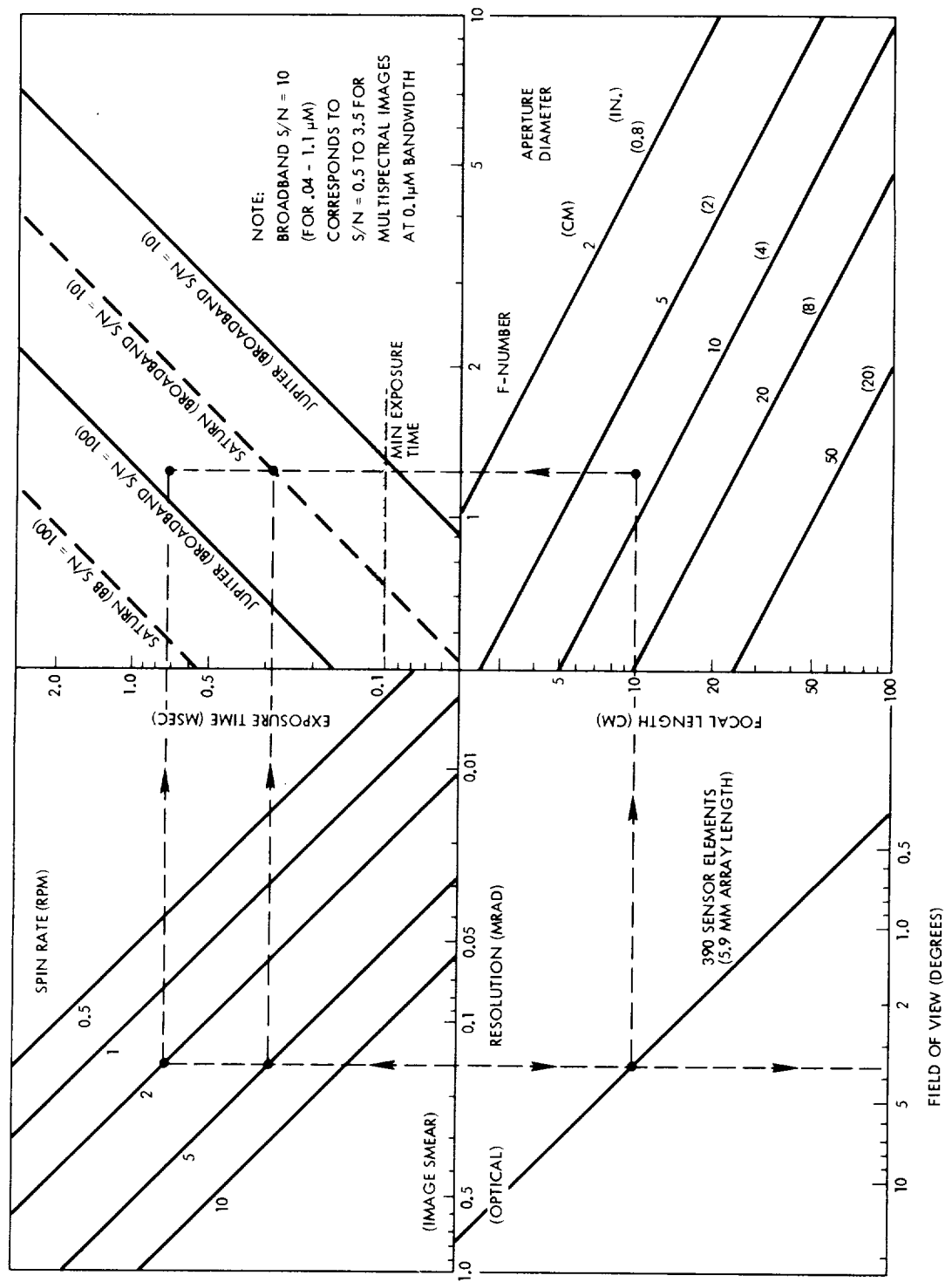Figure A-5. Simulated Imagery of Europa from Close Range

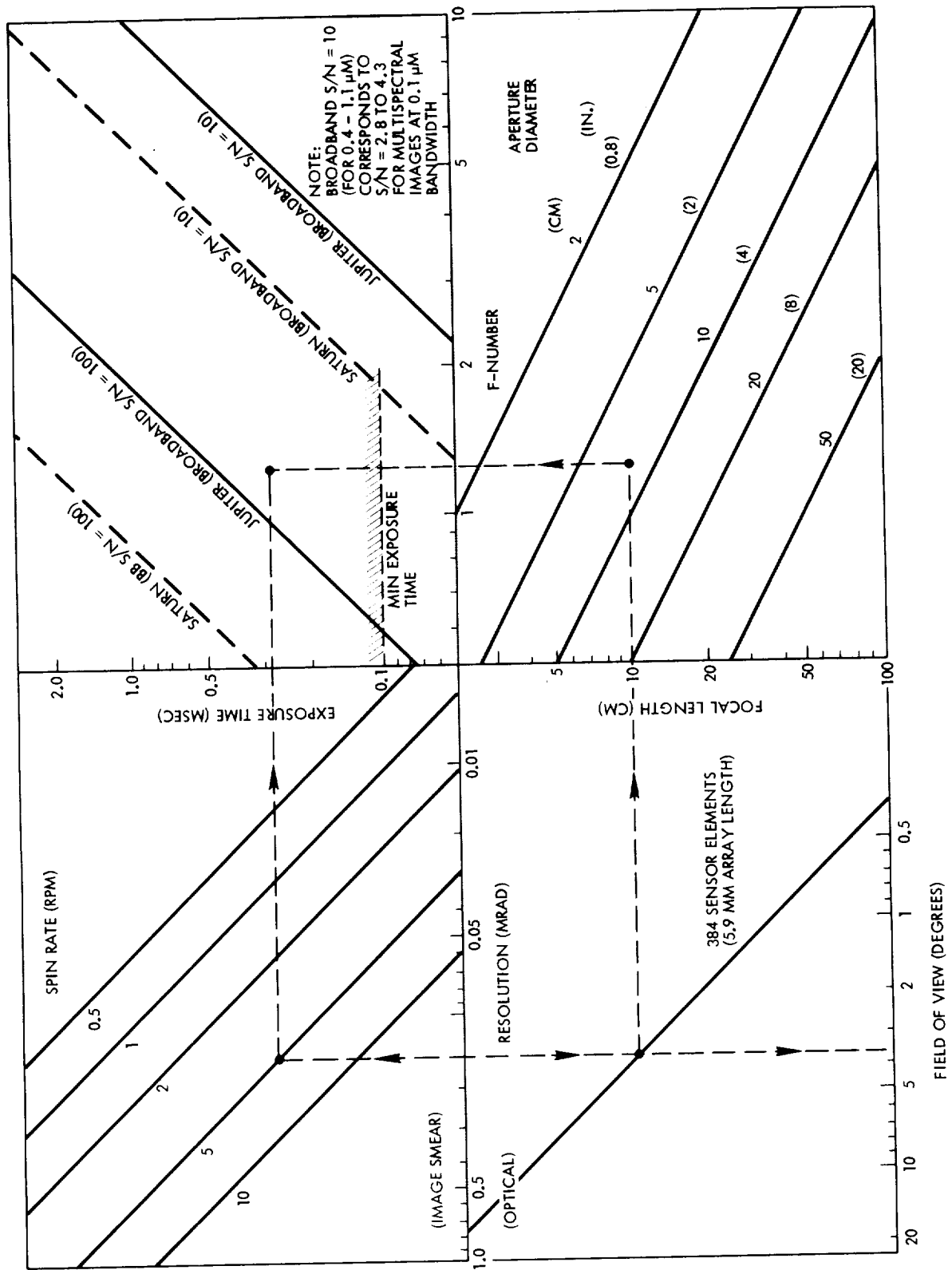Figure A-6. Imaging System Performance in Observation of Jupiter and Saturn Using Phototransistor Array

Figure A-7. Imaging System Performance in Observation of Jupiter and Saturn Using Photodiode Array

APPENDIX B

MISSION ANALYSIS

This appendix presents supporting analyses of spacecraft orbital maneuver characteristics and related performance data referred to in Sections 6 and 7.

1. ORBIT INSERTION MANEUVER REQUIREMENTS AT JUPITER AND SATURN

The orbit dimensions $\alpha = r_a/r_0$ and $\beta = r_p/r_0$, the relative apoapsis and periapsis distances normalized with respect to the planet's surface radius r_0, are related to the hyperbolic arrival velocity V_∞ and the orbit insertion velocity increment ΔV by the equation

$$\alpha = \frac{\beta}{\beta \left[\sqrt{\frac{1}{\beta} + (V_\infty/V_{eo})^2} - \Delta V/V_{eo} \right]^2 - 1} \qquad (B-1)$$

Since the velocity terms are also normalized, using the surface escape velocity $V_{eo} = (2\mu/r_0)^{1/2}$ as reference quantity, this equation describes orbit insertion characteristics at any planet and is the basis of the nomographs (Figures 6-16 and 7-8) shown in Sections 6 and 7 for Jupiter and Saturn, respectively. It follows that ΔV and V_∞ values giving the same orbit dimensions α, β at Jupiter and Saturn are related in the same proportion, namely

$$\Delta V_{SAT} = \frac{V_{eo\ SAT}}{V_{eo\ JUP}} \Delta V_{JUP} = 0.605\ \Delta V_{JUP}$$

$$V_{\infty\ SAT} = \frac{V_{eo\ SAT}}{V_{eo\ JUP}} V_{\infty\ JUP} = 0.605\ V_{\infty\ JUP}$$

Thus the two nomographs, Figures 6-16 and 7-8, are quite similar, except for rescaled values of the velocities ΔV and V_∞.

The orbit periods indicated along the dashed parameter lines of the two graphs are also rescaled, accordingly, by

$$\frac{T_{SAT}}{T_{JUP}} = \frac{r_{o\ SAT}}{r_{o\ JUP}} \cdot \frac{V_{eo\ JUP}}{V_{eo\ SAT}} = 1.398.$$

Equation (B-1) defines changes in orbit insertion velocity ΔV that are required to keep the orbit dimensions α, β invariant with changes in arrival velocity V_{∞}. For example, an increase in V_{∞} would require a corresponding increase in ΔV to attain the same apoapsis α as in the initially assumed case for a specified periapsis β. To derive the equivalent change in ΔV, equation (B-1) is rewritten in the form

$$F = \sqrt{\frac{\alpha}{\beta\ (\alpha+\beta)}} - \sqrt{\frac{1}{\beta} + \left(\frac{V_{\infty}}{V_{eo}}\right)^2} + \frac{\Delta V}{V_{eo}} = 0 \qquad (B-2)$$

The curves representing $F = 0$ in the nomographs, Figures 6-16 and 7-8, are left invariant if a change in V_{∞} from $V_{\infty\ 0}$ to $V_{\infty\ 1}$ is accompanied by the change in ΔV

$$\frac{\delta\Delta V}{V_{eo}} = \sqrt{\frac{1}{\beta} + \left(\frac{V_{\infty\ 0}}{V_{eo}}\right)^2} - \sqrt{\frac{1}{\beta} + \left(\frac{V_{\infty\ 1}}{V_{eo}}\right)^2} \qquad (B-3)$$

Curves of $\delta\Delta V$ as function of β for fixed values of $V_{\infty\ 1}$, with the nominal value $V_{\infty\ 0}$ assumed as 6 km/s, are shown in Figures 6-17 and 7-9 for Jupiter and Saturn orbit injection, respectively.

Consider as an example a change from V_{∞} = 6 km/s to 9 km/s in the case of Jupiter orbit insertion (Figure 6-16). With ΔV = 1.5 km/s and a periapsis radius of 3 R_J (β = 3) the apoapsis radius would be 50 R_J (α = 50), and the orbit period 17 days. As shown in Figure 6-17, the increase of V_{∞} to 9 km/s is equivalent to a reduction of ΔV by 0.62 km/s at β = 3. Thus, a ΔV increase by this amount would be required to attain the same apoapsis as before. With the ΔV value left unchanged, the attainable apoapsis radius would increase to 150 R_J, and the orbit period to 70 days.

2. MANEUVERS TO CHANGE APOAPSIS AND PERIAPSIS RADIUS

Maneuver velocities to change the apoapsis or periapsis radius are given by

$$\Delta V_p = V_{eo} \sqrt{\frac{r_o}{r_p}} \left(\sqrt{\frac{r_{a1}}{r_p + r_{a1}}} - \sqrt{\frac{r_{a2}}{r_p + r_{a2}}} \right) \qquad (B-4)$$

$$\Delta V_a = V_{eo} \sqrt{\frac{r_o}{r_a}} \left(\frac{r_{p1}}{r_{p1} + r_a} - \sqrt{\frac{r_{p2}}{r_{p2} + r_a}} \right) \qquad (B-5)$$

respectively, where

ΔV_p = periapsis maneuver to change the apoapsis from r_{a1} to r_{a2}

ΔV_a = apoapsis maneuver to change the periapsis from r_{p1} to r_{p2}

Figures B-1 and B-2 give Jupiter orbit velocities at periapsis and apoapsis from which the ΔV requirements can be conveniently determined.

Equations (B-4 and (B-5) show that rescaling by the ratio

$$\frac{V_{eo\ SAT}}{V_{eo\ JUP}} = 0.605$$

yields the corresponding orbit change maneuver velocities at Saturn.

For example, an apoapsis change from 20 to 30 Jupiter radii at $r_p = 3\ R_J$ requires a ΔV of 700 m/s (Figure B-1). The corresponding maneuver at Saturn requires only 425 m/s. A periapsis change from 3 to 2 R_J at an apoapsis distance of 50 R_J requires a ΔV of 360 m/s at Jupiter, and 220 m/s at Saturn.

A chart for convenient assessment of ΔV requirements for orbit modification is shown in Figure B-3. The data given in this chart are based on the assumption of Hohmann transfers by cotangential maneuvers at periapsis and at apoapsis.
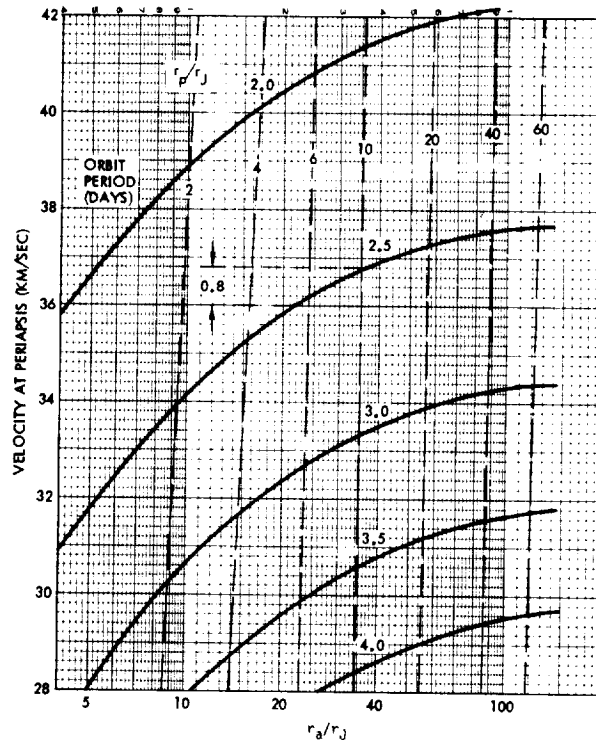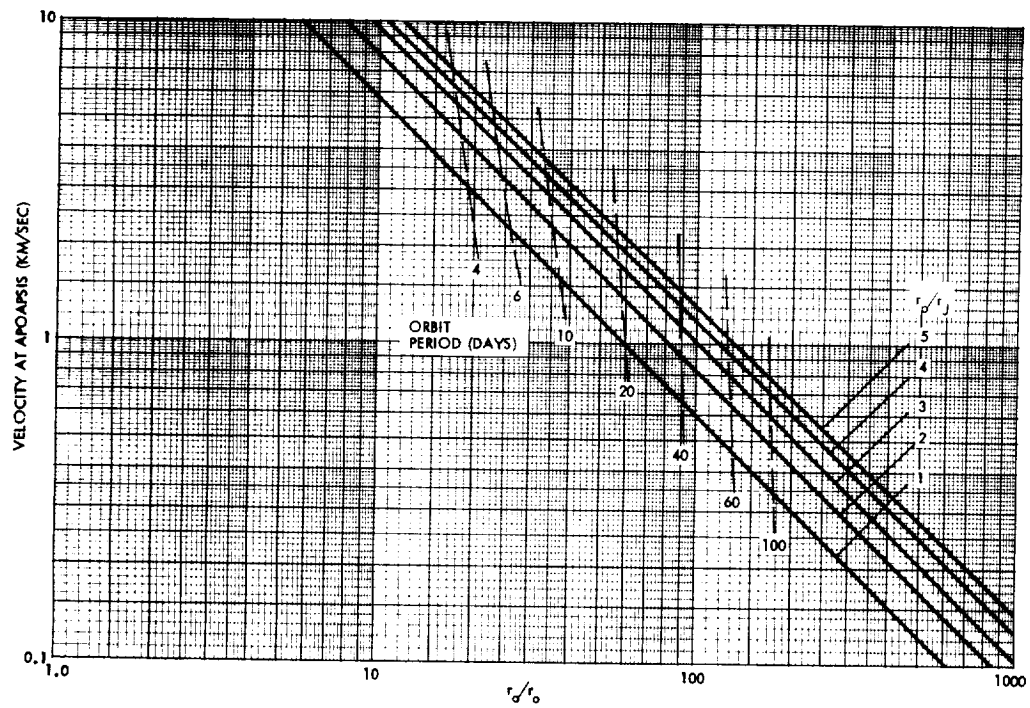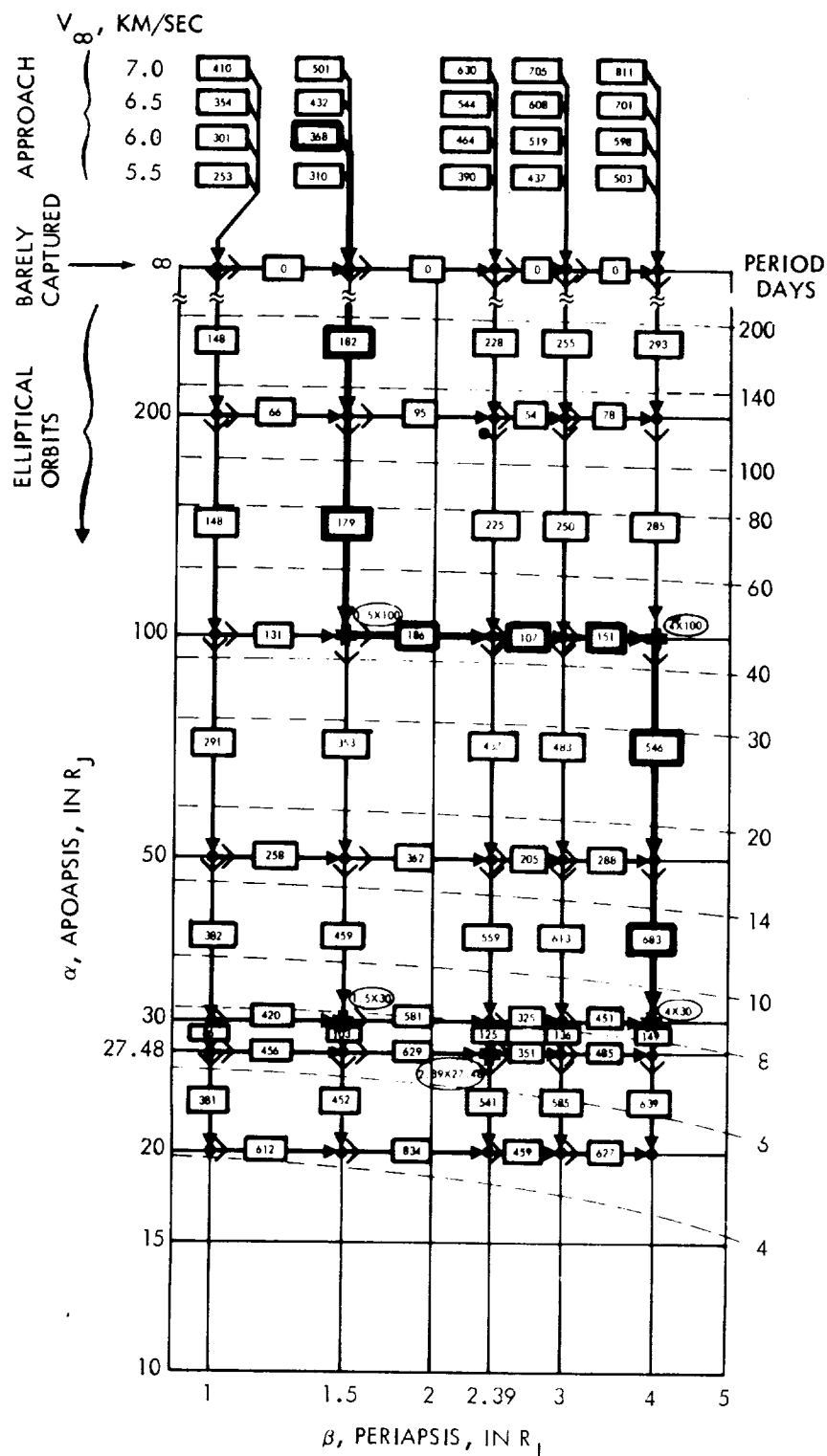
Figure B-1. Periapsis Velocities at Jupiter

Figure B-2. Apoapsis Velocities at Jupiter

B-4

Figure B-3. Jovian Orbit ΔV Chart

It can be observed that orbit modification by this sequence:

1) raising periapsis by posigrade thrusting at apoapsis

2) lowering apoapsis by retrograde thrusting at periapsis

always results in a lower total ΔV requirement than by the reversed sequence.

Actually, the constraint of earth line orientation of the spacecraft +Z axis implies that large apoapsis and periapsis maneuvers can only be performed in the directions indicated under items 1) and 2) above. This fact must be taken into consideration in orbit modification planning.

3. ORBIT INSERTION IN EARTH-POINTING MODE

As discussed in Section 6.8.3 it is desirable to perform the orbit insertion maneuver while in the earth-pointing mode.

To satisfy this requirement, the angles ZAE (from $\overline{S}$ vector to earth line) and γ (from $\overline{S}$ vector to optimum thrust line) must be nearly supplementary as illustrated in Figure B-4. For simplicity it is assumed here that the earth line is coplanar with the common plane of the hyperbolic approach trajectory and the elliptical orbit. ZAE is a function of arrival date, and γ is a function of β and V_∞, also a function of arrival date. The above constraint on γ and ZAE is thus essentially a constraint on the arrival date.

From Figure B-4, the angle γ through which the approach trajectory is deflected from asymptote to periapsis is obtained by

$$\csc \gamma = 1 + \frac{\beta\, r_o}{a} = 1 + 2\beta \left(\frac{V_\infty}{V_{eo}}\right)^2 \tag{B-6}$$

the deviation of the optimum thrust line (tangential to the trajectory at periapsis) from the earth line is given by

$$\Delta = 180^\circ - \text{ZAE} - \gamma \tag{B-7}$$

Figure B-5 shows the change in arrival conditions in terms of the angles 180° - ZAE and γ for several values of β as function of flight time, for
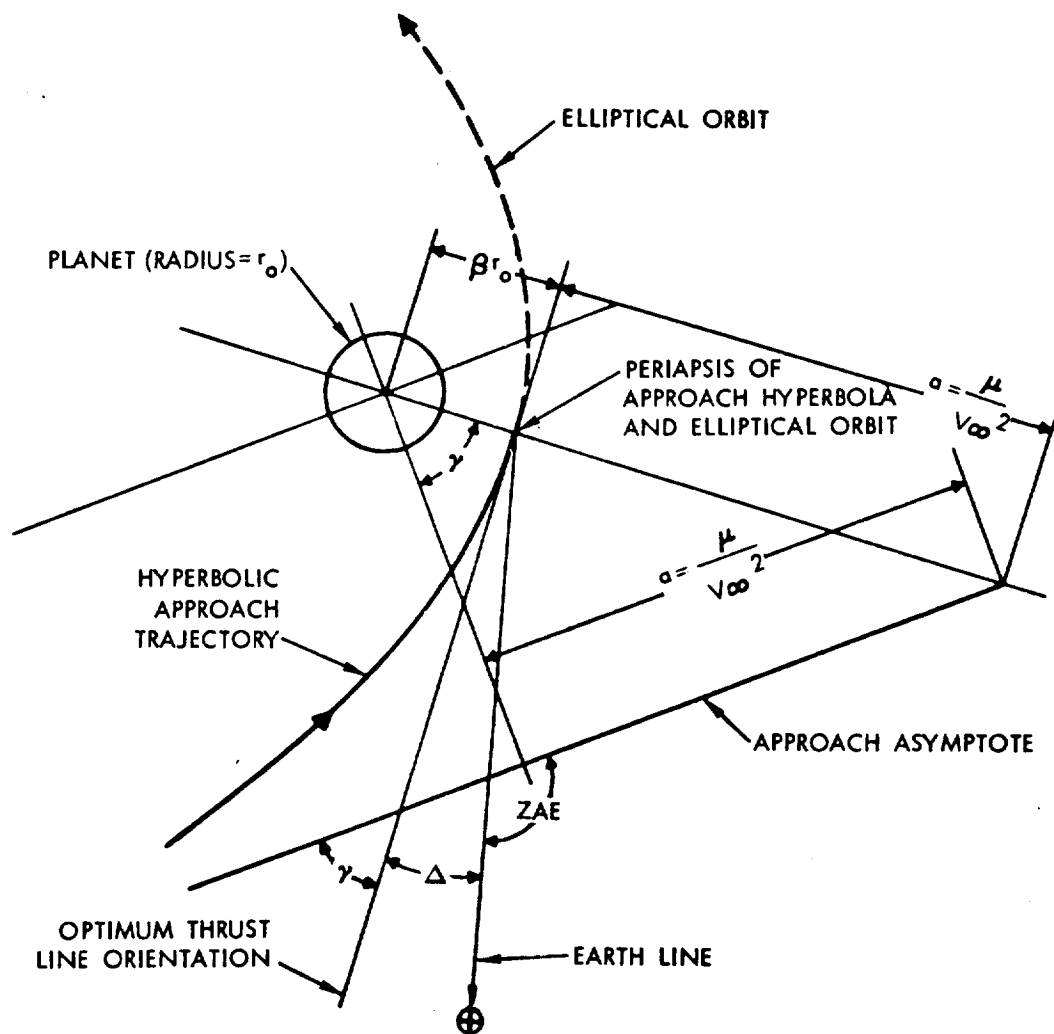
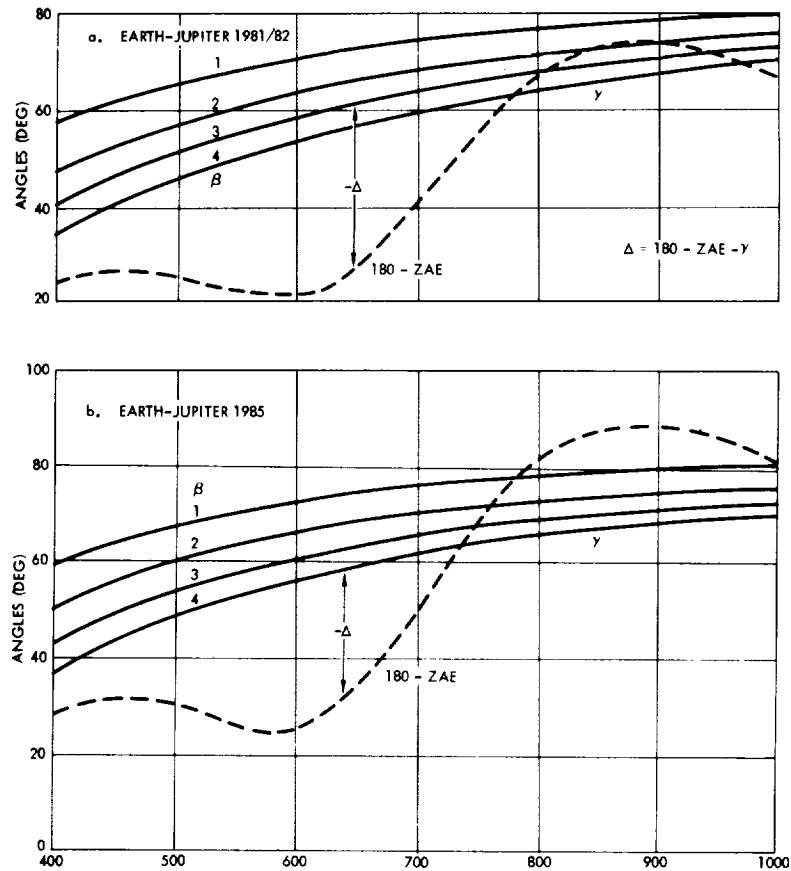Figure B-4. Geometry of Earth-Line Orbit Insertion

Figure B-5. Deviation Angle Δ of Tangent at Periapsis
from Earth-Line Vs. Trip Time
(1981 and 1985 Jupiter Missions)

1981 and 1985 earth-Jupiter trajectories. The deviation angle Δ and,
hence, the cosine-loss of maintaining the spacecraft in the earth-pointing
mode during the maneuver attains small values at flight times between
750 and 950 days depending on β. The results shown in Figure 6-19 (Sec-
tion 6) for β = 3 were derived from these data.

The corresponding results for 1982 and 1986 earth-Saturn trajectories
are shown in Figure B-6. Here the deviation angle Δ attains small values
at short flight times (<900 days) as well as long flight times (1500 to
1900 days), depending on β. However, the short flight time case is of no
interest because of the excessive departure and arrival hyperbolic veloci-
ties involved. Results shown in Figure 7-12 (Section 7) for β = 3 were
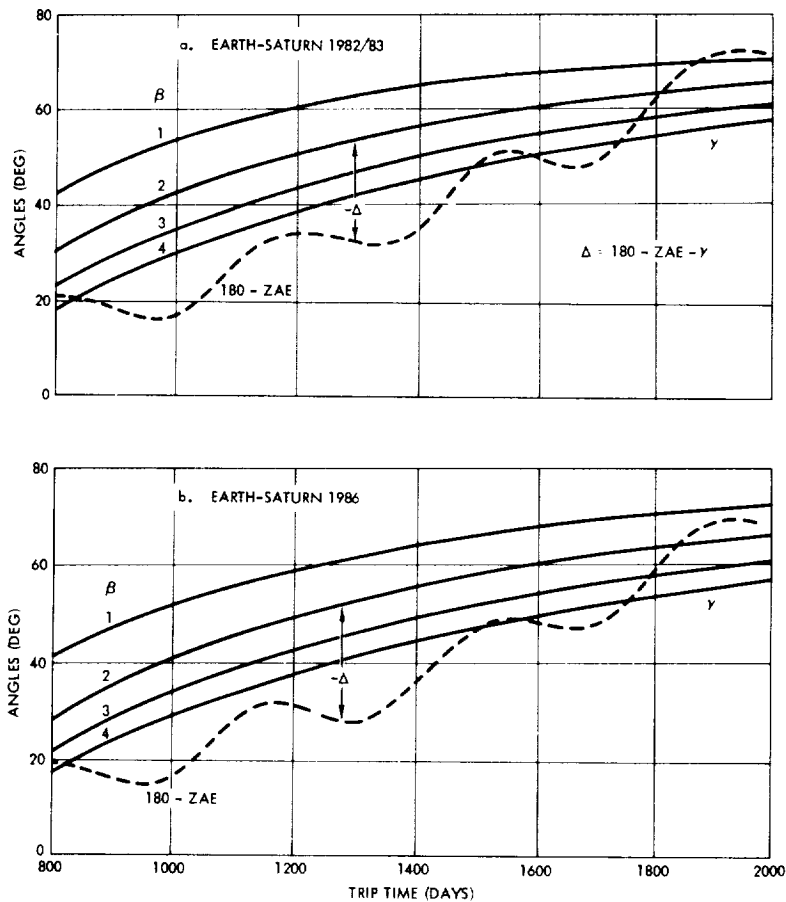derived from the above data.

B-8

Figure B-6. Deviation Angle Δ of Tangent at Periapsis
from Earth-Line Vs. Trip Time
(1982 and 1986 Saturn Missions)

4. COSINE-LOSSES FOR NONCOPLANAR ORBIT INSERTION

The earth-pointing requirement may entail an orbit insertion maneuver which is out of the plane of the approach hyperbola. This can occur, for example, if a highly inclined capture orbit is desired. Suppose the aim angle in the impact parameter plane is chosen such that the post-encounter trajectory has an inclination i_1 with respect to Jupiter's orbit plane. Then the periapsis velocity can be resolved into two components, in-plane and perpendicular to Jupiter's orbit plane.

Earth pointing means a direction approximately parallel to the ecliptic, thus the ΔV expended by the spacecraft will in the worst case provide the component

$$\Delta V' = \Delta V \cos i_1$$

B-9

for orbit insertion purposes. To achieve a specified orbit size, the ΔV expenditure must therefore be increased accordingly, namely in the ratio of $1/\cos i_1$ compared to coplanar injection.

Figure B-7 shows the apoapsis radius achievable at Jupiter as a function of the out-of-plane angle i_1 and the corresponding orbit period, with ΔV as parameter. The figure shows curves for periapsis distances of 1, 2 and 3 R_J. The arrival velocity is assumed to be 6 km/s. Cosine losses exhibited by these graphs begin to increase very rapidly as inclination angles exceed 20 degrees.

5. ORBIT PERTURBATIONS

Orbit perturbations due to the oblateness of Jupiter and Saturn primarily involve the rotation of the line of nodes and the line of apsides. The nodal regression is expressed by

$$\dot{\Omega} = -\frac{3}{2}\frac{n\,J_2}{a^2\,(1-e^2)^2}\cos i \tag{B-8}$$

the apsidal rotation by

$$\dot{\omega} = -\frac{3}{4}\frac{n\,J_2}{a^2\,(1-e^2)^2}\,(4 - 5\cos^2 i) \tag{B-9}$$

In these equations

$$n = n_0\left(\frac{r_0}{a}\right)^{3/2}$$

$$n_0 = \sqrt{\frac{\mu}{r_0^3}} = \begin{array}{l}2920.7 \text{ deg/day for Jupiter}\\3318.1 \text{ deg/day for Saturn}\end{array}$$

and $J_2 = 0.0147$ for Jupiter, 0.0167 for Saturn. In the case of Jupiter the equations can be rewritten as

$$\frac{-4\,\dot{\omega}}{4 - 5\cos^2 i} = -2\,\dot{\Omega}/\cos i = 91.055\,\frac{(\alpha + \beta)^{1/2}}{(\alpha\beta)^2} \quad \text{(in deg/day)} \tag{B-10}$$
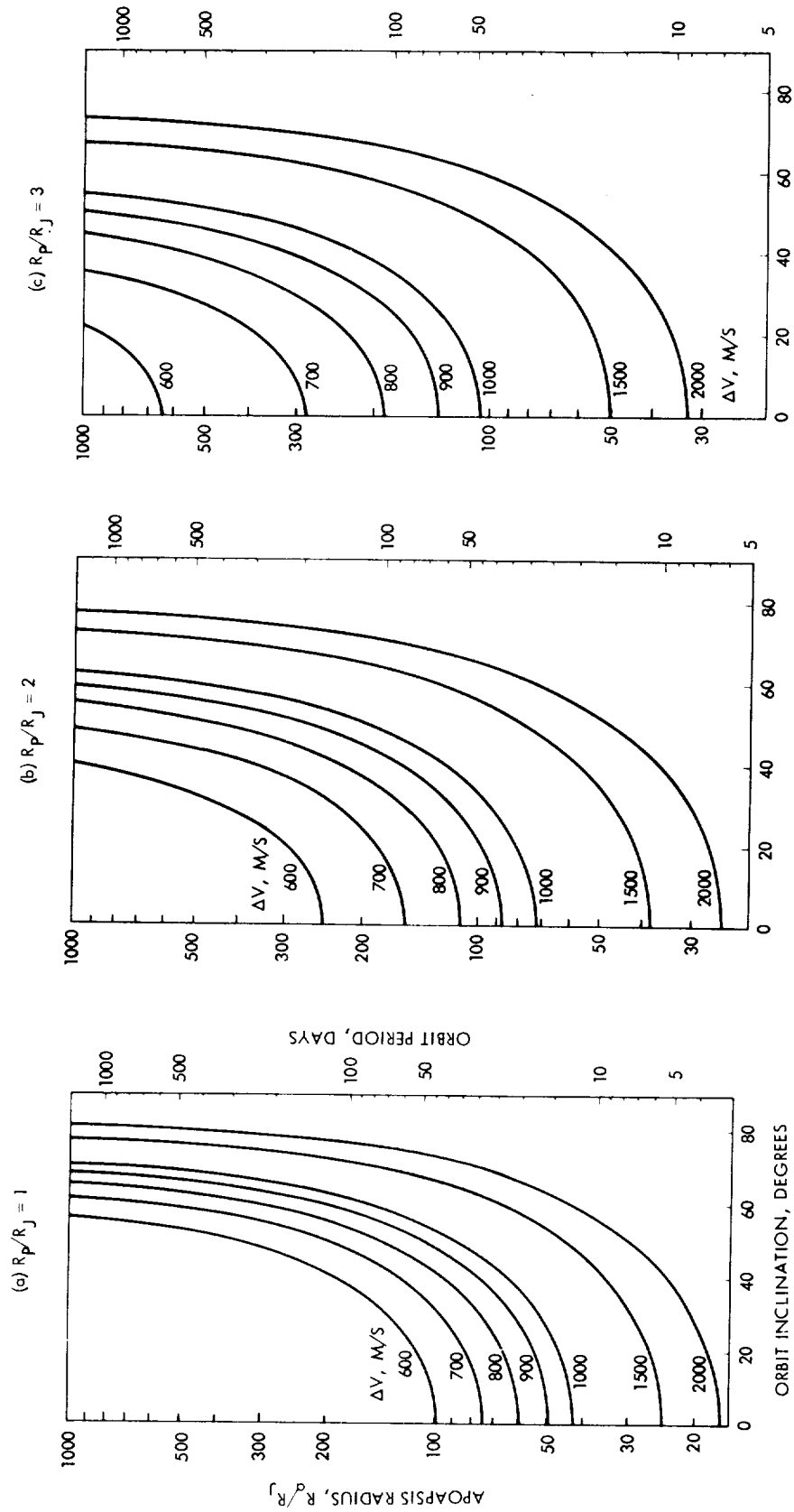
B-10

Figure B-7. Velocity Requirements for Injection into Inclined Orbits at Jupiter (Impulsive orbit insertion while earth pointing; V_∞ = 6 km/s)

where α and β are the normalized apoapsis and periapsis distances. In the case of Saturn the coefficient of the term on the right side is to be replaced by 103.44.

Figure B-8 shows these rotation rates parametrically in a diagram of orbital dimensions α and β for Jupiter orbits. Conversion of the diagram to Saturn orbits only requires a scale change of the rotation rate coefficients indicated along the parameter lines by the ratio
103.44 ÷ 91.055 = 1.136.

$$\dot{\omega}/(\frac{4-5\cos^2 i}{4}) = -2\dot{\Omega}/\cos i \ (^\circ/day)$$
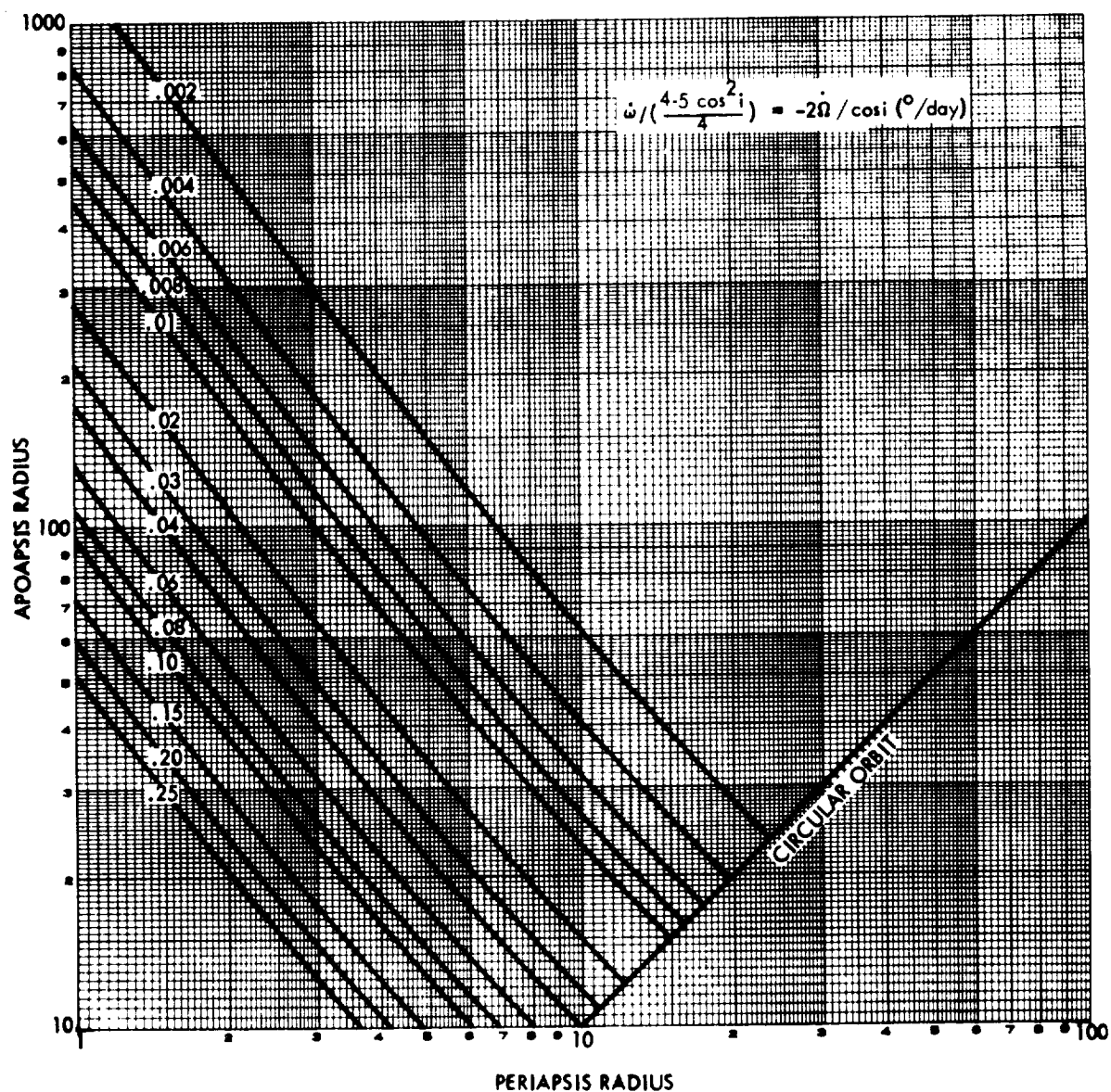
CIRCULAR ORBIT

APOAPSIS RADIUS

PERIAPSIS RADIUS

Figure B-8. Rotation Rates of the line of Nodes and Line of Apsides in the Equatorial Plane of Jupiter

For representative orbit sizes considered here the rotation rates are very small. Thus, for a 3 x 40 R_J Jupiter orbit of 30 degrees inclination the nodal regression rate is 0.0173 degree/day; the apsidal advance is 0.0025 degree/day. The rates would be 14 percent greater for a corresponding orbit around Saturn.

6. SENSITIVITY OF ORBIT DIMENSIONS TO INJECTION POINT DISPERSION

The effect of navigation errors accrued prior to injection on the parameters of the capture orbit was discussed in Section 6.11. The following analysis determines the uncertainty of capture orbit size resulting from 1) uncertainty of the actual periapsis distance at which the orbit insertion maneuver is performed, and 2) uncertainty of the actual velocity V_p attained by the maneuver. This velocity uncertainty is due partly to inaccurate knowledge of the arrival velocity, and partly to inaccurate control of the velocity increment ΔV.

For a gross estimate of the orbit dimension uncertainty we shall only consider the sensitivity of the apoapsis with respect to variations of periapsis radius and velocity.

The sensitivity $\partial r_a / \partial r_p$ for fixed velocity V_p is given by

$$\frac{\partial r_a}{\partial r_p} = \frac{r_a}{r_p} \left(\frac{2 r_p + r_a}{r_p} \right) = m (2 + m) \qquad (B-11)$$

where $m = r_a / r_p$.

The sensitivity $\partial r_a / \partial V_p$ for fixed r_p is given in terms of the dimensionless quantities $\alpha = r_a / r_0$, $\beta = r_p / r_0$, and $\nu_p = V_p / V_{esc_0}$, namely

$$\frac{V_{esc_0}}{r_0} \frac{\partial r_a}{\partial V_p} = \frac{\partial \alpha}{\partial \nu_p} = 2 \sqrt{\beta^3 m (1 + m)^3} \qquad (B-12)$$

Taking into account the surface escape velocities at Jupiter (60.2 km/s) and Saturn (36.4 km/s) we observe that the sensitivity $\partial \alpha / \partial V_p$ is 1.653 times greater in the case of Saturn orbits. The sensitivity $\partial r_a / \partial r_p$ is the same for any planet.

Figures B-9(a) and (b) show the sensitivities $\partial r_a/\partial r_p$ and $\partial r_a/\partial V_p$ as functions of r_a for several fixed values of r_p. For highly eccentric orbits with small periapsis and large apoapsis radii, typical of the missions being considered, the sensitivities are very large, with $\partial r_a/\partial r_p$ ranging from 100 to 200 and $\partial r_a/\partial r_p$ ranging from 50 to 100 planet radii per km/s. A periapsis dispersion of the order of 0.01 planet radii (600 to 700 km) thus leads to an apoapsis dispersion of 1 to 2 planet radii, and a velocity uncertainty of 10 m/s leads to an apoapsis uncertainty of 0.5 to 1 planet radii. These uncertainties are to be combined in an RSS sense.
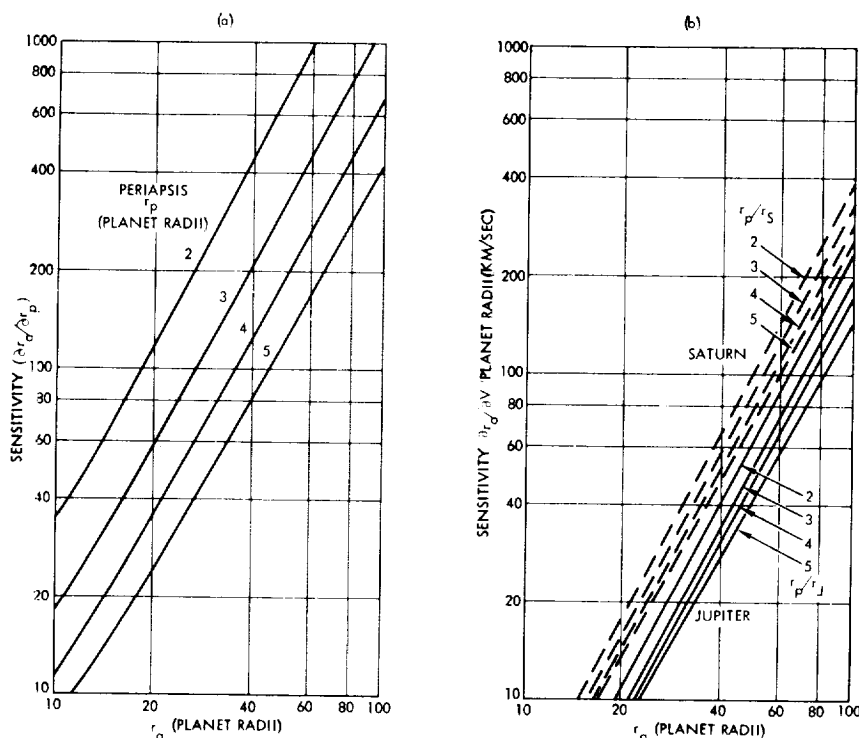

Figure B-9. Apoapsis Sensitivity to (a) Periapsis Distance and (b) Velocity

It is also of interest to consider the sensitivity of the orbital period to these variations. From the equation which defines the orbital period

$$T_p = 2\pi\sqrt{\frac{a^3}{\mu}} = \frac{\pi r_0}{V_{esc_0}}\sqrt{(\alpha + \beta)^3}$$

B-14

the sensitivity with respect to variation of the apoapsis distance obtained, viz.,

$$\frac{\partial T_p}{\partial \alpha} = \frac{3}{2} \frac{\pi r_0}{V_{esc_0}} \sqrt{\alpha + \beta}$$ (B-13)

or, in normalized form,

$$\frac{1}{T_p} \frac{\partial T_p}{\partial \alpha} = \frac{3}{2} \frac{1}{(\alpha + \beta)}$$ (B-14)

Figure B-10 shows the sensitivity $\partial T_p/\partial \alpha$ of Jupiter and Saturn orbits as function of apoapsis distance α for periapsis distances of 2 and 4 planet radii. Typically, a variation of α by 1 planet radius causes a 2 to 5 percent variation of the orbit period, or 0.5 to 1.5 days for typical orbit dimensions at Jupiter and Saturn.

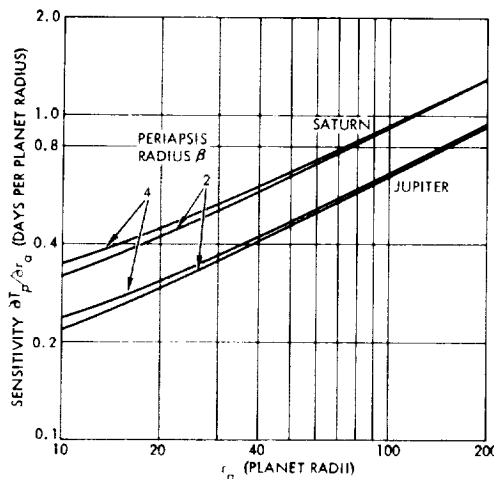Figure B-10. Orbit Period Sensitivity to Variation in Apoapsis Radius

APPENDIX C

ELECTRONIC PIECE PARTS FAILURE RATES

Pioneer F/G failure rate data of electronic piece parts referred to in Section 5.6 of this document are given in Table C-1.

Table C-1. Pioneer F&G Project:
Basic Parts Failure Rate List

Part Type	Failure Rate (30°C and 25 percent Electrical Stress) Failure/10^9 Hours	Failure Mode Distribution	
		% Short	% Open
Integrated Circuits			
RTL	25	30	70
DTL	25	30	70
Analog amp.	100	30	70
MOS	100	--	--
Hybrid	150	--	--
TTL	25	--	--
Transistors			
Silicon, low power	10	60	40
Silicon, high power	40	60	40
Field effect	60	60	40
Diodes			
Silicon, general purpose	3	60	40
Zener	37	75	25
4-layer devices (SCR, etc.)	136	80	20
Varactor	40	60	40
Tunnel	100	--	--
Silicon power rectifier	44	60	40
Resistors			
Carbon composite	2	0	100
Metal film	1	0	100
Wire wound (power, pre- cision, etc.)	10	10	90
Variable, wire wound	50	10	90
Thin film resistor network	50	60	40
Capacitors			
Ceramic	4	50	50
Glass	3	60	40
Polystyrene	30	60	40
Filters, feed-through	10	95	5
Tantalum, solid	9	85	15
Tantalum, foil	20	60	40
Variable	40	60	40
Mica	4	60	40
Mylar	20	60	40

Part Type	Failure Rate (30^0C) and 25 percent Electrical Stress) Failure/10^9 Hours	Failure Mode Distribution	
		% Short	% Open
Magnetic amplifier	14	50	50
Transformer	14	50	50
Inductors (per coil)	10	20	80
Relays			
Non-latching	106	50	50
Latching	64	50	50
Fuse	100	0	100
Connector, coaxial	10	0	100
Connector pin, active	0.1	0	100
Connection, welded	0.5	0	100
Solar cell	1	0	100
Thermister	35	10	90
Crystals, quartz	20	--	--
Lamp	200	0	100
Switch, snap-action	250	10	90
Thermal switch	80	50	50
Core, magnetic	0.01	--	--

Table C-1. Pioneer F&G Project: Basic Parts Failure Rate List
(Continued)

Part	Failure Rate ($30^{0}C$ and 25 percent Electrical Stress) Failure/10^9 Hours
Tank	0.6 per in. of weld
Bladder	330
Fill valve, cap	70
Pressure transducer, leakage	70
Pressure transducer, non-performance	5
Thermostat	56/cycle
Thermostat switch	70
Heater blanket	17
Heater strip flexible	14
Leak detector, open	10
Leak detector, short	100
Squib valve, leakage	100
Squib valve, firing (mission)	66
Pressure switch, leakage	300,000
Pressure switch, non-performance	20
Check valve	140/cycle
Tubing	58
Pressure seals (V-seals and O-rings)	0.6/inch
Mechanical connections (MS fittings)	100
Squib pin puller (mission)	5
Separation nut, explosive (mission)	300,000
Cable assembly	48,000
Stud (mission)	438
Hold-down spring	500
Hold-down arm	110
Hold-down latch	100
Torsional spring	100

Table C-1. Pioneer F&G Project: Basic Parts Failure Rate List (Continued)

Part	Failure Rate (30°C and 25 percent Electrical Stress) Failure 10^9 Hours
Leaf spring	220
Ratchet latch	110
Elastic bumper	100
Paddle hinge assembly	100
Hinge joint	662
Compression spring	100
Damper	450
Pin pull release device	48,000
Pin	100
Shear pin	6
Filter	24
Fuel regulator	400
Solar paddle structure	100
Boom structure	100
Boom hinge assembly (mission)	600,000
Hydraulic damper, viscous	500

APPENDIX D

STRUCTURAL LOADS ON APPENDAGES DUE TO COMBINED SPIN
AND THRUST EFFECTS

The axial loads on spacecraft appendages induced by high thrust application interact with the radial loads caused by the centrifugal effect due to spinning. This interaction becomes more pronounced as the spin rate is increased and has the effect of stiffening the deployed appendages against bending due to axial spacecraft accelerations. Bending moments and boom deflections are reduced as a result, and compressive loads in the lower guide rods of the RTG deployment arms due to bending are decreased because of the superimposed centrifugal tension. As discussed in Sections 3.5, 3.6 and 3.7 these factors as well as the increased spacecraft spin stability achievable at increased spin rate favor operation at 15 rpm during high thrust maneuvers.

1. REDUCED BOOM DEFLECTION DUE TO SPIN STIFFENING

The bending deflection of a cantilevered boom (Figure D-1) is reduced due to the addition of a radial force at the tip mass. Boom mass is neglected in this analysis. The result is given by

$$h_1 = \frac{h_0}{1 + \frac{F_r}{F_a} \frac{h_0}{L}}$$

where

h_0 = deflection of boom in absence of radial force F_r

h_1 = deflection of boom for radial force $F_r \neq 0$

F_r, F_a = radial and axial forces applied to tip mass
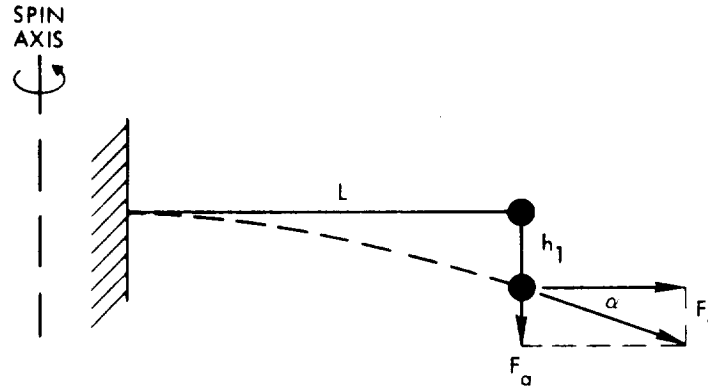
L = boom length.

Figure D-1. Cantilevered Boom under Axial and Radial Load

Figure D-2 shows the deflection ratio h_1/h_0 as function of the force ratio F_r/F_a with the normalized deflection h_0/L as parameter. The tilt angle α of the resulting force at the end mass is given by

$$\alpha = \tan^{-1}(F_a/F_r),$$

also indicated at the abscissa of the graph. For $F_a/F_r = 5$ (or $\alpha = 12$ degrees) the deflection h_1 is only about 65 percent of h_0 if the parameter h_0/L is 0.1. For a very flexible appendage (such as the magnetometer boom) the effect is much more pronounced, with h_1/h_0 reduced to about 30 percent at the same force ratio F_a/F_r if $h_0/L = 0.4$.

At 20 rpm the force ratio is about 1/10 for the 10-foot RTG booms and 1/20 for the 20-foot magnetometer boom, assuming a worst-case axial acceleration of 0.125 g (100 lb_f of thrust, empty tanks).

The non-dimensional expression h_1/h_0 also appears in the equation which gives the reduction of the maximum bending moment at the root of the boom:

$$M_1 = F_a L - F_r h_1 = M_0 \left(1 - \frac{h_1}{h_0}\right)$$

where M_1 and M_0 designate the moments with and without F_r. A second scale on the ordinate of Figure D-2 indicates this result. Thus in the second example above a deflection of 30 percent of h_0 corresponds to a reduction of M_0 by 30 percent.
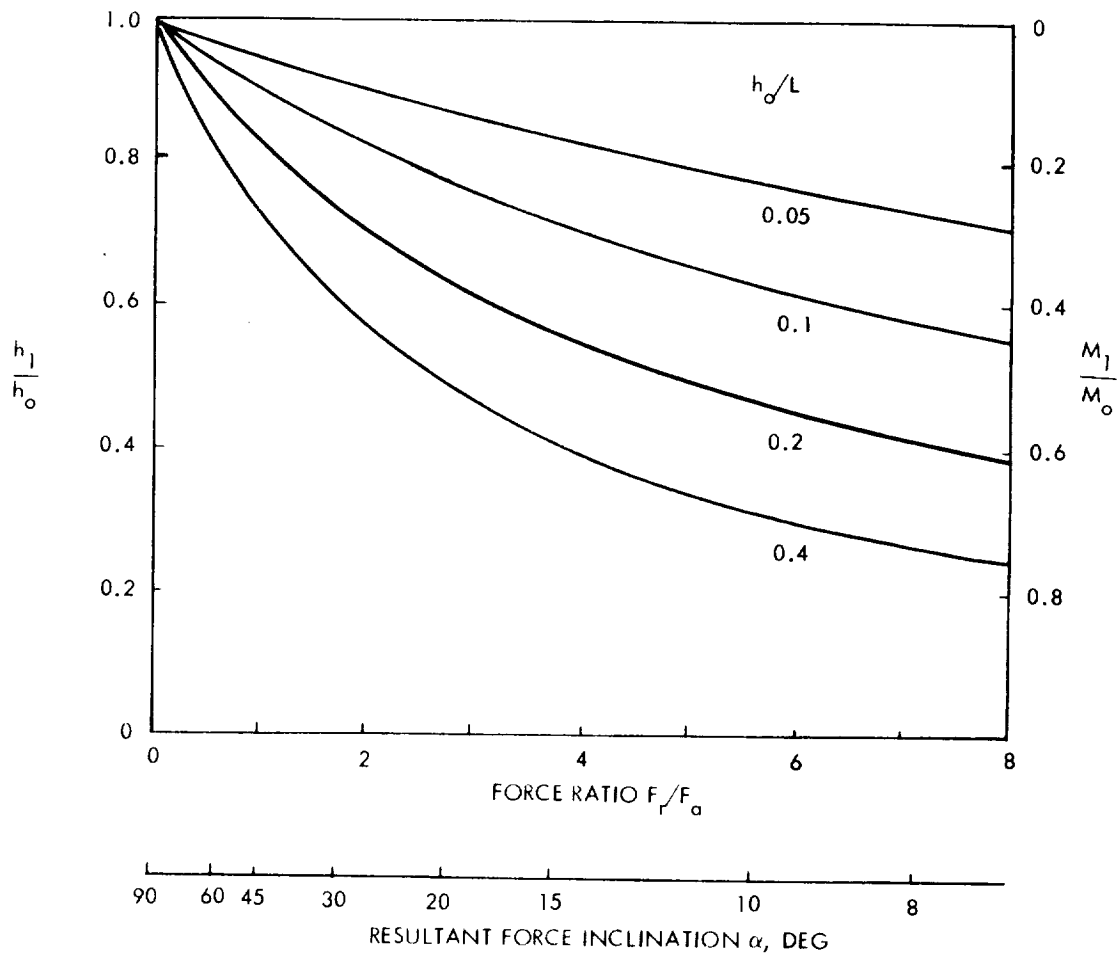
Figure D-2. Effect of Spin Stiffening on Tip Deflection and
Maximum Bending Moment of Cantilever Beam

Bending moments and boom deflections of the Pioneer F/G magnetometer boom under axial and radial loads are actually characterized by a model which differs slightly from the simple cantilever configuration illustrated in Figure D-1. Rather than being clamped at the root the magnetometer boom is hinge-mounted and free to rotate in the X-Z plane up to ±3 degrees from the nominal X-axis alignment. Thus, if the resultant force inclination α is less than 3 degrees, i.e., if the axial force F_a is less than 5.23 percent of the radial force F_r, the boom will align itself along the resultant force line without experiencing a bending moment. (The small spring force introduced by the wobble damper can be neglected.) With an axial force larger than this limit value only the excess amount $F_a - 0.0523\ F_r$ will contribute a bending moment and, hence, a boom deformation. For example,

D-3

in the case of a 0.1 g axial acceleration and 15-rpm spin rate (1.4 g radial acceleration of the tip mass) the bending moment at the root of the magnetometer boom is reduced by 72 percent, from 600 to 170 inch-pounds, as a result of the hinged/clamped support action described above. This indicates that the simplified clamped cantilever model shown in Figure D-1 gives conservative estimates of boom moments in the range of axial loads actually encountered in the high thrust maneuver mode.

Figure D-3 schematically illustrates the stiffening effect at low and high spin rates as a result of the vector combination of the axial (F_a) and radial (F_r) reaction forces that are applied at the appendage end masses. Typically, the deflection of the magnetometer boom due to a 0.1 g axial acceleration is reduced by about 50 percent if the spin rate is increased from 4.8 to 10 rpm.
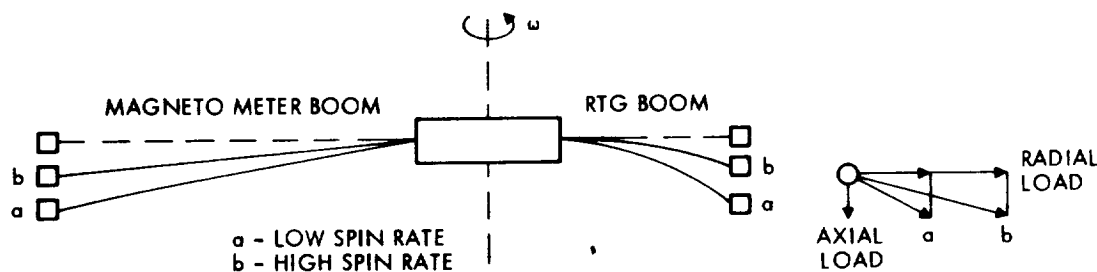

Figure D-3. Effective Stiffening of Appendages due to Increase in Spin Rate (Schematic)

The interaction also tends to keep the tip deflection of the magnetometer boom and the RTG booms approximately equal, so that asymmetry of mass distribution due to boom deflection, and hence tilting of the principal axis of inertia is minimized. Preliminary analysis shows that the worst-case tilt angle occurring for a 100 lb_f thrust and empty propellant tanks is about 0.5 degrees at 10 rpm and only about 0.25 degree at 15 rpm.

2. EFFECT ON BUCKLING LOADS ON LOWER RTG GUIDE RODS

Increasing the spin rate also has the advantage, from a structural load standpoint, of increasing the tensile stress in the guide rods of the RTG deployment arms. Since the tensile load increases with the square

of the spin rate, the net compressive load acting on the lower guide rods as a result of bending of the deployed structure due to axial thrust can be greatly reduced as illustrated in Figure D-4. Thus, the safety margin of these long, slender rods against buckling is effectively increased. A preliminary analysis of this effect is given below.
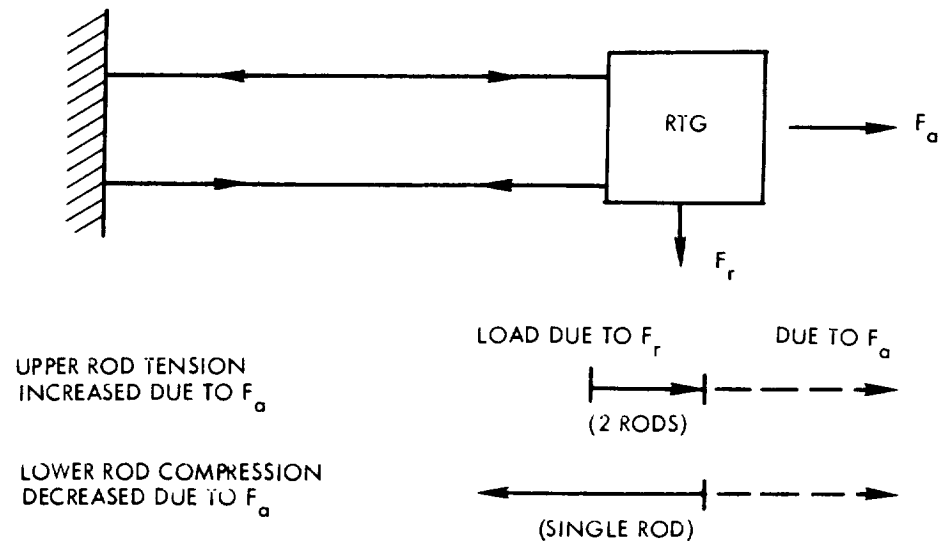

Figure D-4. Tensile and Compressive Loads on RTG Guide Rods

The critical buckling load in the lower guide rods, assumed as pinned and clamped at their ends, is expressed by

$$P_{crit} = 2\pi^2 \ EJ/L^2$$

The dimensions of the Pioneer F&G RTG rods are

L = 2060 mm

D = 15.9 mm (outer diameter of tube)

d = 14.5 mm (inner diameter of tube).

Thus $J \cong 0.05 \ (D^4 - d^4) = 950 \ mm^4$. Assuming $E = 7000 \ kg/mm^2 \cong 10^7$ psi for Aluminum 6061 we obtain a critical buckling load of 70 pounds for this rod. Figure D-5 shows the variation of compressive load with spin rate for three values of thrust force. The second scale on the ordinate gives

the percentage of critical load. At the nominal spin rate of 4.8 rpm and with 100 lb_f of thrust, the rod is loaded to 75 percent of the critical value, at 15 rpm only to 50 percent. At 25 rpm the compressive load is cancelled by the tensile load. These results indicate the desirability of spinning up to 15 rpm if the Pioneer F&G rod dimensions are used.
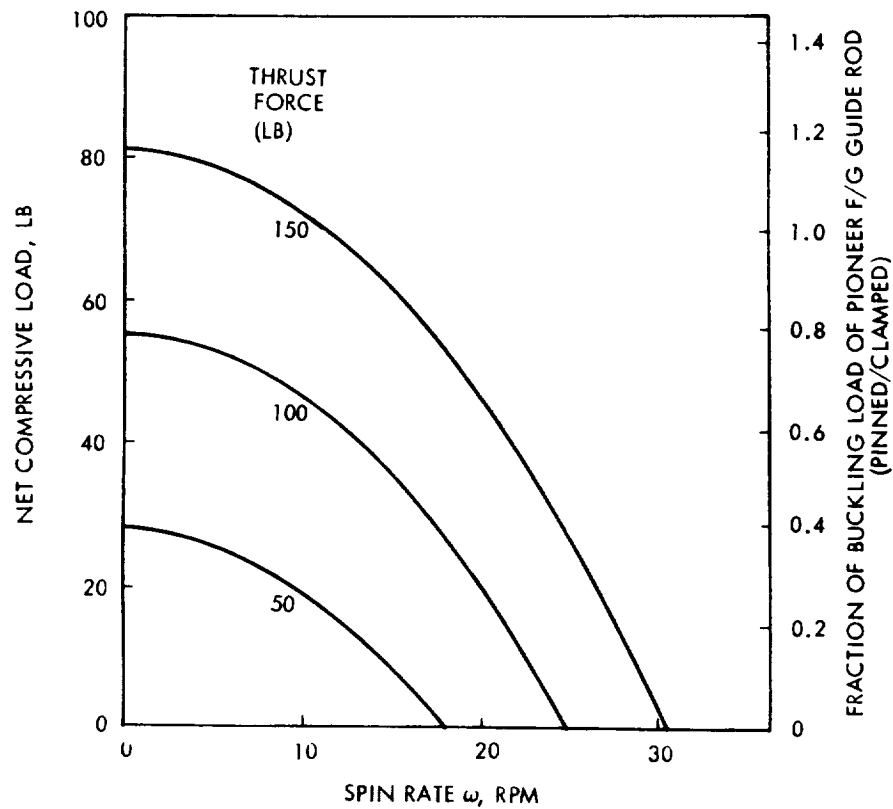

Figure D-5. Worst Case Net Compressive Load on Lower Pioneer F/G
Guide Rod Due to Axial and Radial Acceleration

The increase in tensile load and stress of the upper RTG rods with spin rate is illustrated in Figure D-6. Even at 25 rpm this load (and the resulting stress of 1700 psi) is quite insignificant.
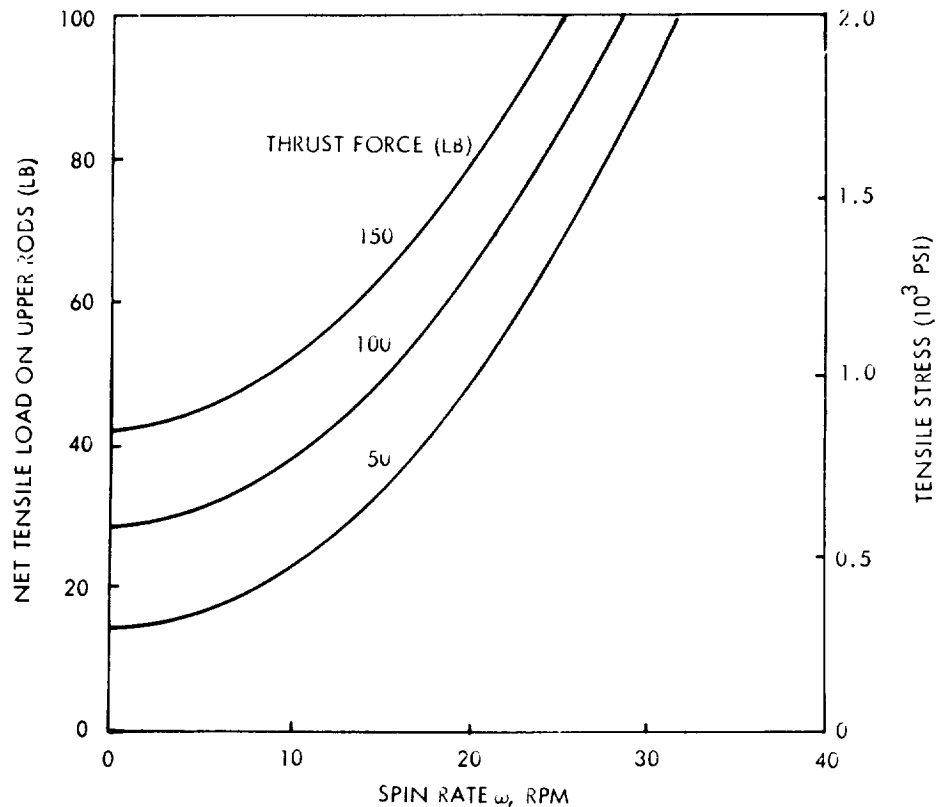
Figure D-6. Worst Case Net Tensile Load on Upper RTG Guide Rods

3. BENDING OF RTG BOOM AND GUIDE RODS

The model used to analyze bending effects due to F_a is sketched in Figure D-7. For simplicity we assume the rods to be pinned at the base and clamped at the RTG side. The maximum bending stress in each rod in this case is given by

$$\sigma_{B_{max}} = \frac{1}{3}\frac{F_a L}{Z}$$

and would be 37,000 psi if the Pioneer F&G tubular rods with a section modulus $Z = 120 \text{ mm}^3$ are used unchanged. Depending on the details of rod attachment on both ends the maximum stress may actually be considerably less, e.g., only 18,500 psi with both ends of the rod clamped. To these stresses a tensile or compressive stress component of 1000 psi corresponding
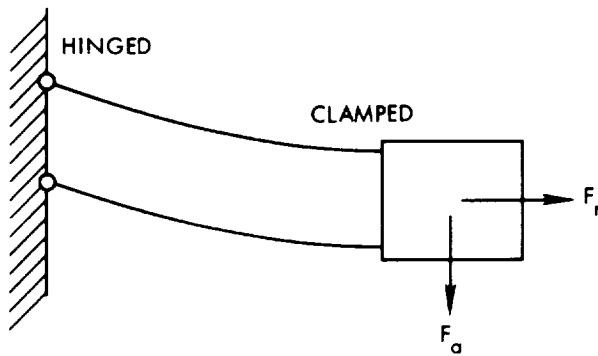
Figure D-7.   RTG Boom Bending Model

to a 15 rpm spin rate must be added.   Some stress reduction due to
the effect discussed previously is to be anticipated.   On the other hand,
the existence of significant buckling loads in the lower rods requires an
adequate safety factor (about 1.5).

Without more detailed analysis it appears that the worst case
stresses are too high for aluminum rods, and reinforcement by increasing
the wall thickness is to be contemplated.   Figure D-8 shows the reduction
of stresses by increasing the wall thickness from the present 0.7 mm to
1.5 mm.   The figure also shows the corresponding total weight increment
of the six rods.   A 1.5 mm wall thickness is probably more than adequate,
reducing the maximum bending stress to 20,000 or 10,000 psi, respectively,
for the conservative and the less conservative assumptions on rod attach-
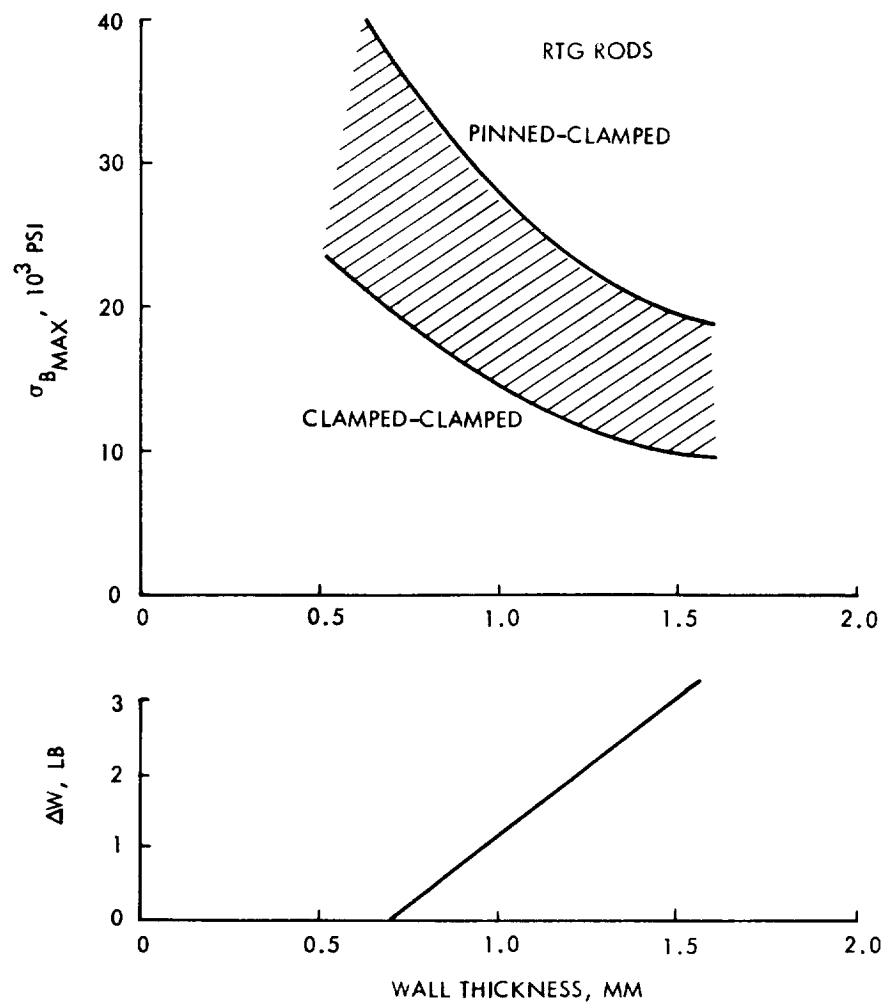ment made here.   The total weight increment is only 3 pounds in this case.

Figure D-8. RTG Rod Reinforcement by Increased Tube Wall Thickness

APPENDIX E

CANDIDATE RTG POWER SOURCES

Three candidate RTG systems were evaluated for their application to the Pioneer Outer Planets Orbiter: 1) Pioneer SNAP-19, 2) SNAP-19 HPG System, and 3) multi-hundred-watt (MHW) system. A summary of their characteristics is presented in Table E-1.

Table E-1. Candidate RTG Systems

Parameter (per unit)	Pioneer SNAP-19	MHW	HPG SNAP-19
Thermal loading (W)	645	2200	1025
Power output (W)			
Beginning of life (BOL)	40	150	69
Launch plus two years	36	143	62
Launch plus five years	31	135	56
Percent power in air	100	53	100
BOL conversion efficiency (%)	6.2	6.8	6.9
Load voltage (V)	4.2	28	6.7
Weight (lb)	30.0	65	38.4
BOL specific power (W/lb)	1.33	1.77	1.8
Envelope (in.)			
Diameter	15.7	15.6	23.8
Length	11.2	22.9	13.4
Availability	1971	1975	1975
Unit Cost ($K)*	130	400	225
Status	Pioneer F/G hardware	Hardware technology evaluation in progress	Study phase (not funded)
Technology	Proven	Ambitious	Same as SNAP-19

*Repetitive hardware costs for one unit. Price assumes fueled capsule of required size will be provided GFE by the AEC

1. PIONEER 10/11 SNAP-19

Two of the Pioneer 10/11 SNAP-19 RTG units are shown in Figure E-1. The design differs from that used on the Nimbus spacecraft in several ways. The p-material has been changed to TAGS-85 (0.15 AgSbTeGe, 0.85 GeTe) and the end closures of the sealed generator are welded rather than bolted

and sealed with a double o-ring. In addition, the heat source uses tantalum-based refractory metals in place of the super alloy heat source used by Nimbus SNAP-19's. The 90 couples in the SNAP-19 have been re-configured for Pioneer into a 2 x 45 series-parallel arrangement with an output voltage of 4.2 volts.
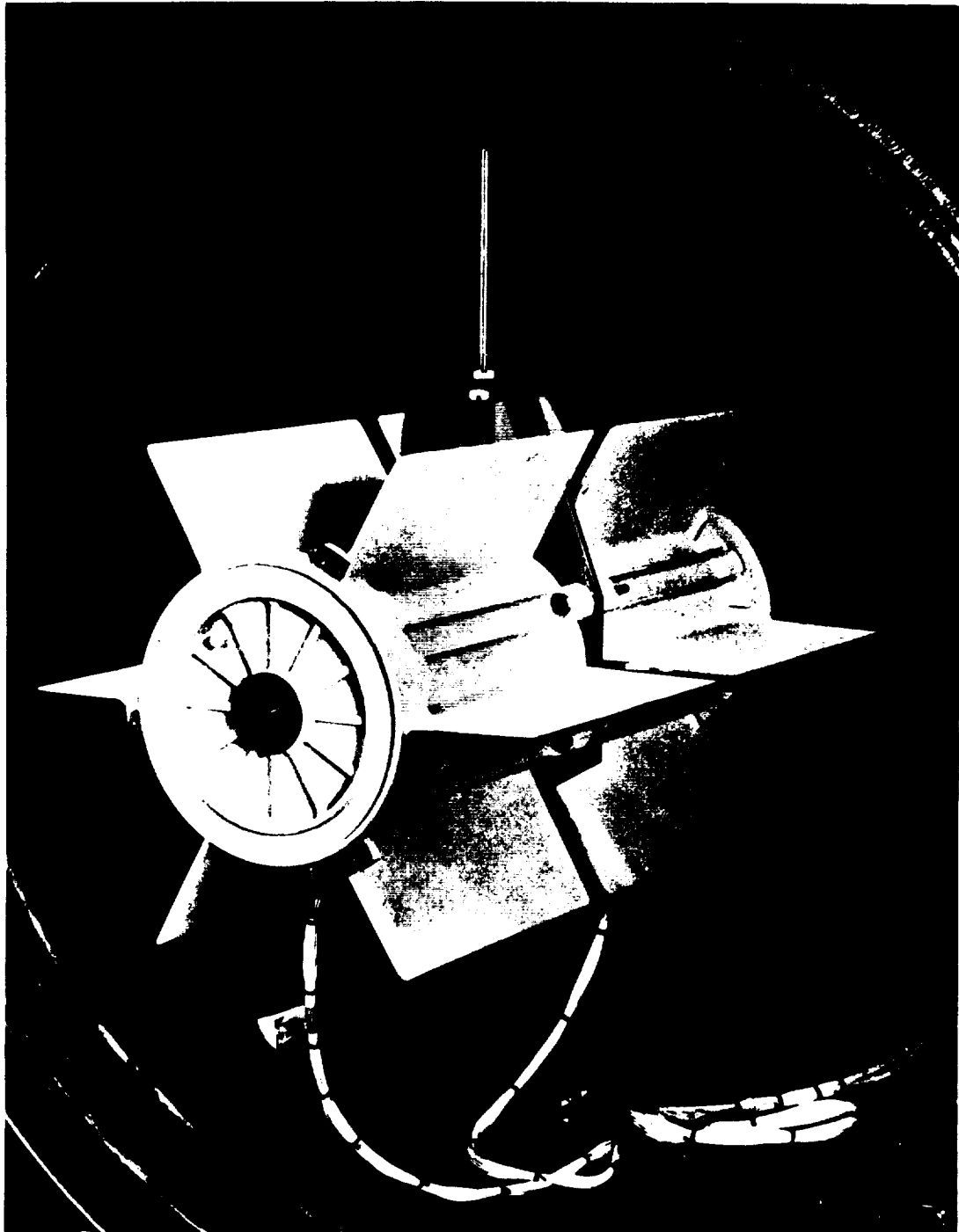

Figure E-1. Pioneer SNAP-19 RTG

Four RTG units, grouped in pairs as shown in Figure E-1, power the Pioneer 10/11 spacecraft. The specified power at launch is 37.9 watts for each of two outboard RTG's and 37.5 watts for inboard RTG's. The difference in output is caused by the higher operating temperatures of the inboard unit. The specified unit degradation rate is 0.22 watt/month.

Figure E-2 shows the specified power output of the four SNAP-19 RTG units versus time compared to the performance actually measured during the first 21 months of operation on Pioneer 10 and the first 18 months of operation on Pioneer 11. The performance of the Pioneer 10 units exceeds specification by as much as 10 to 15 watts, that of the Pioneer 11 units by about half as much. Even more encouraging, the measured output data (averaged so as to eliminate the apparent fluctuations due to telemetry readout levels) conform with a degradation rate of about 5 percent per year. This rate is predicted on the basis of RTG performance test data.
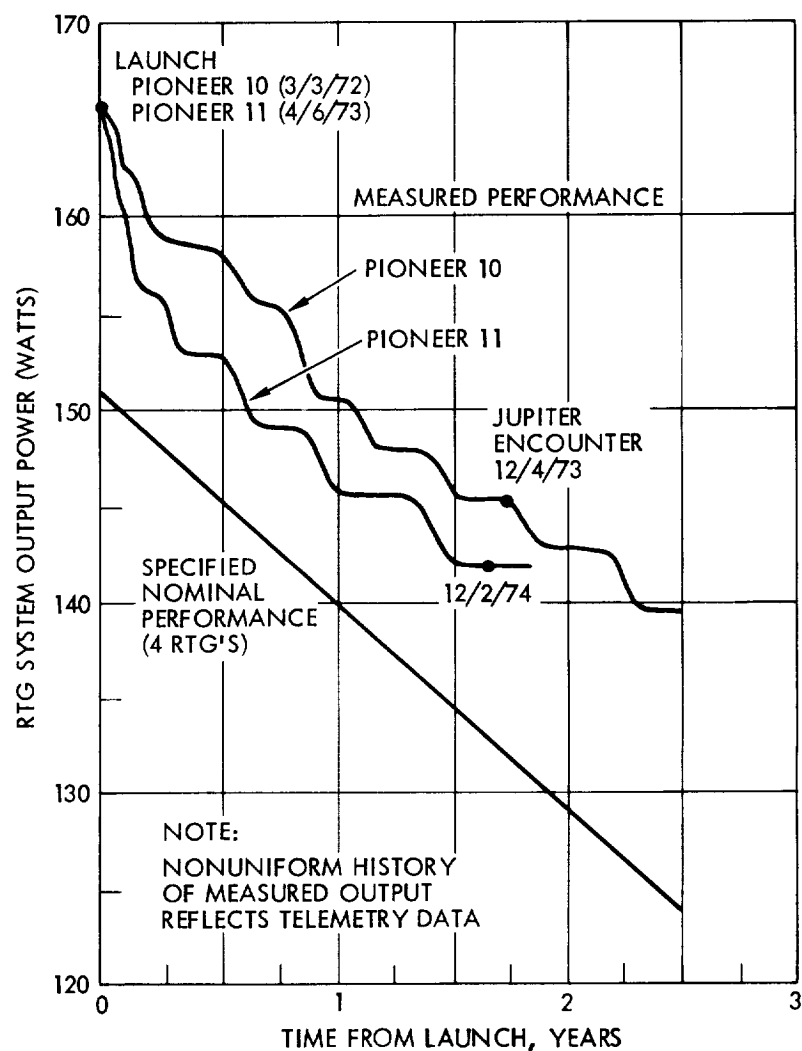

Figure E-2.   Specified and Measured Performance
of Pioneer SNAP-19 RTG's

2. SNAP-19 HIGH PERFORMANCE GENERATOR (HPG)

The HPG is essentially a scaled-up SNAP-19 design. It will have improved power-to-weight characteristics (specific power), a redesigned heat source, and a superior gas seal. The heat source loading has been increased to 1025 thermal watts to increase the electrical power output to 69 watts, and the fins have been extended to maintain a fin root temperature of 330°F. The HPG system is shown in Figure E-3.

TELEDYNE ISOTOPES
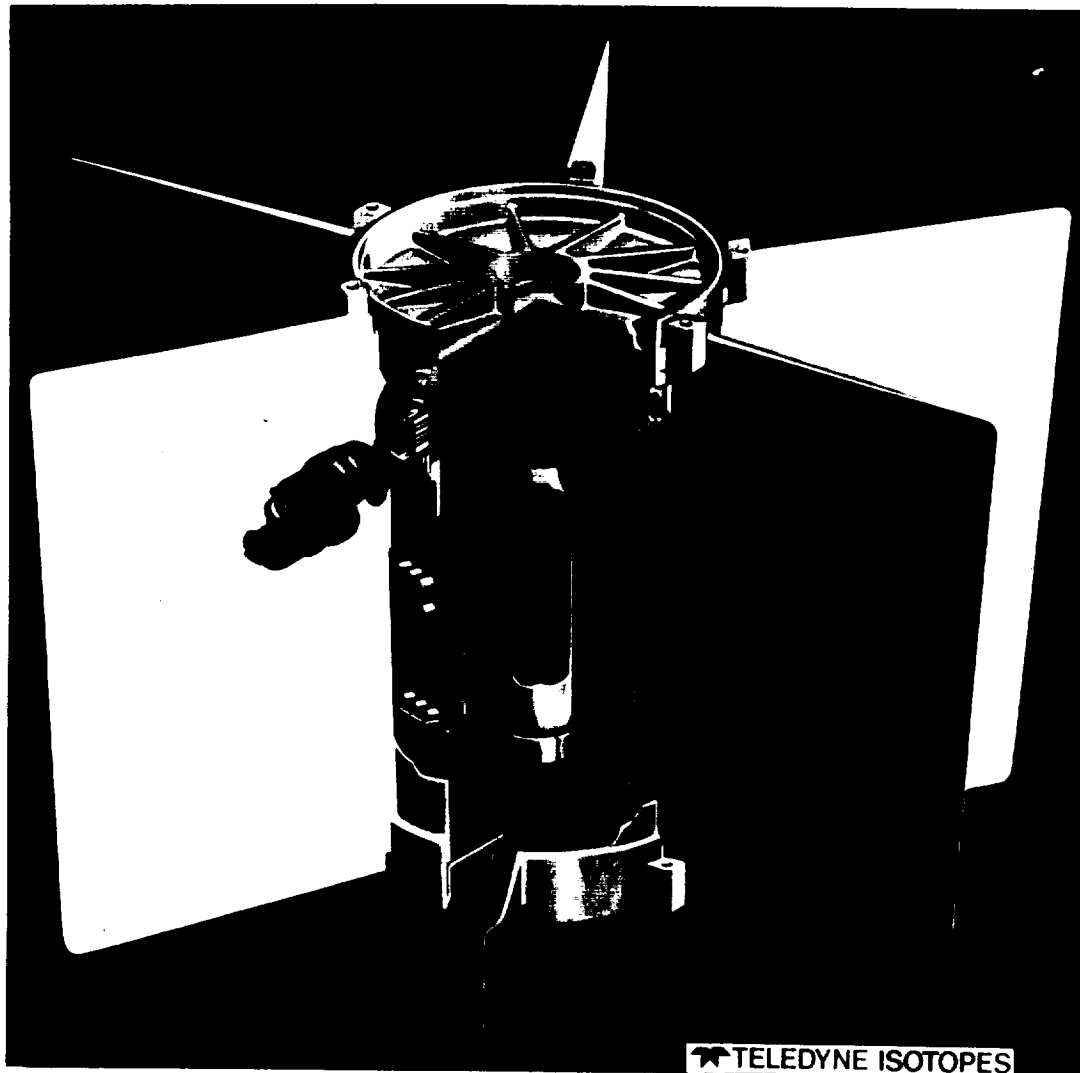
Figure E-3. High Performance Generator (HPG) SNAP-19 RTG

A prototype unit (HPG S/N 1) utilizing a TZM electrical heat source in place of the nuclear fuel capsule has been subjected to an endurance test during the past year. Extrapolation of power output/initial power data obtained thus far confirm the superior life expectancy of the HPG system compared to the SNAP-19 Pioneer.

A summary of the design characteristics for the Pioneer SNAP-19 and SNAP-19 HPG are given in Table E-2.

E-4

Table E-2. Comparison of SNAP-19 RTG Characteristics

	Pioneer SNAP-19	HPG SNAP-19
T/E Couples	TAGS - 85/2N	TAGS - 85/2N
BOL Operating Temperature	980/360°F (HJ/CJ)	995/360°F (HJ/CJ)
Housing Material	Magnesium	Magnesium
Number T/E Couples	90	144
T/E Couple Module Array	3 by 5	2 by 12
Fuel Inventory	645 watt(t)	1025 watt(t)
BOL Power Output	40 watt(e)	69 watt(e)
BOL System Efficiency	6.25%	6.7%
T/E Cold Sink Bar	Aluminum	Aluminum
T/E Cold Sink Spring Piston	Aluminum	Beryllia
Heat Shield Ablation Thickness	0.45"	0.93"
Header Closure	Bolts/Weld	Shear Weld
Weight	30.0#	38.4#
BOL Power to Weight	1.3 w(e)/lb.	1.8 w(e)/lb.
Overall Dimensions	11.15" Lg X 15.68" Dia.	13.4" Lg X 23.8" Dia.
Load Voltage	4.2 volts	6.9 volts
Fin Root Temperature	330°F	330°F

3. MULTI-HUNDRED-WATT (MHW GENERATOR)

The MHW effort is currently a technology program funded by the AEC. The objective is to advance the technology required to achieve a high-performance system in terms of specific power by operating at high temperature. The concept is being developed to meet the increasingly stringent power requirements for a wide spectrum of orbital and deep space missions. The MHW's current specific application is for the LES-8 and -9 earth orbital mission, scheduled for launch in 1974/1975.

The MHW system (Figure E-4) consists of a cylindrical array of air-vac thermocouples surrounding a high-temperature radioisotope heat source. The thermoelectrical material is atomic 80 percent silicon and 20 percent germanium. The converter operates at a nominal hot junction temperature of 2012°F (1100°C) to 1832°F and cold junction temperature of approximately 615°F (324°C). Table E-3 summarizes the converter design parameters. The beginning-of-life power output of the MHW converter is predicted to be 150 + 5 watts, and the beginning-of-life conversion efficiency is predicted as 6.8 percent, at a design hot junction temperature for this system of 2012°F. The temperatures in both the thermoelectric material and the heat source are several hundred degrees above the present state of the art. The thermoelectric material specified in the baseline design, which is the comparatively new 80 percent Si-20 percent Ge material, has a higher melting point than the previously used 63 percent Si-37 percent Ge, but
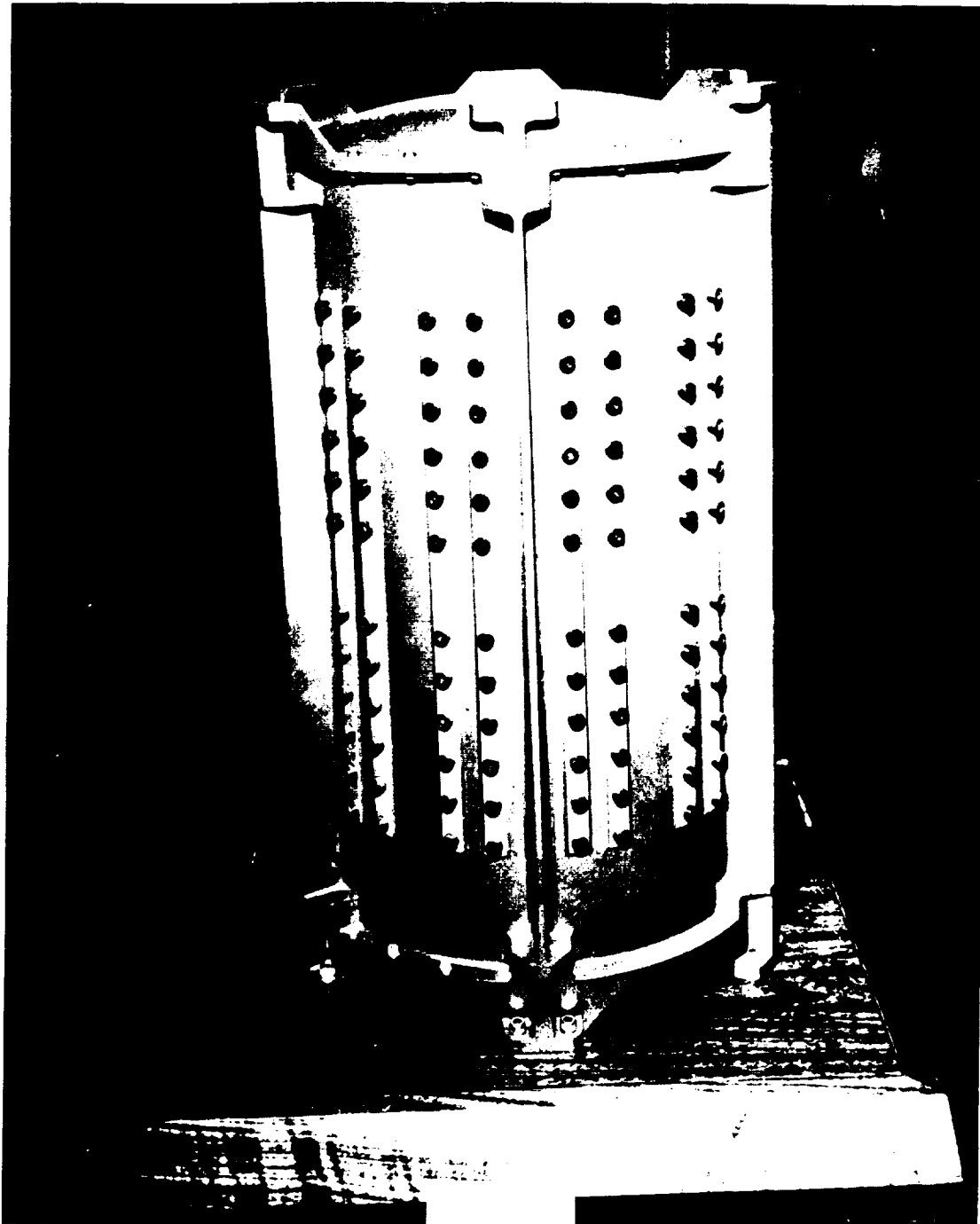
Figure E-4. Multi-Hundred-Watt (MHW) RTG

Table E-3. MHW Converter Design Summary

Beginning of life power output	150 ± 5 watts*
Weight	85 pounds
Hot junction temperature	1832°F
Cold junction temperature	615°F
Load voltage	28 to 30 volts
Efficiency	6.8 percent
Number of couples	288
Number of series - parallel strings	2
Couple length	0.8 inch
N-element diameter	0.164 inch
P-element diameter	0.164 inch
Outside converter diameter	15.6 inches
Converter length	22.9 inches

*Approximately 80 watts of power output is obtained during in-air ground operation

also has accumulated significantly less long-term test data. The insulation specified for the thermoelectric converter is a high-temperature molybdenum multifoil system which must be sealed until after launch to avoid oxidation.

The MHW heat source design uses the spherical ceramic "Siren Capsule" technology developed by Sanders Nuclear Corporation. The ceramic fuel form spheres are surrounded by an Iridium shell and covered with a wound graphite yarn composite structure. These spheres are enclosed in a right circular cylindrical reentry shell which has an inner heat shield of pyrolytic graphite and an outer aeroshell of POCO graphite. The cylinder also contains crushable material to provide additional impact protection and is enclosed in a cladding container to provide air handling capability. This heat source design is referred to as the Helipak heat source concept.

The MHW system should be relatively insensitive to normal prelaunch mechanical stresses, including ground handling, qualification testing, storage, and transportation. The 0.05-inch thick outer shell should be adequate to withstand most of the dangers associated with normal handling. One problem that does exist is possible damage to the cold side of one or more of the thermoelectric couples, which could result in the loss of the necessary sealed converter condition prior to launch. Enough clearance must exist between the heat source and the converter to eliminate possible damage to the elements during launch vibration.

The MHW system's power output is more than adequate for the Pioneer orbiter missions, and the system offers the highest specific power of all candidate systems investigated.

4. RTG SELECTION TRADEOFFS

This section discusses integration considerations, design, development, cost, and availability schedules that influence the selection of a candidate RTG system. A comparison is made of the relative merits of the candidate systems leading to the selection of a preferred configuration for the Pioneer Outer Planets Orbiter baseline.

4.1 Schedule of Development and Availability

The important considerations in selecting an RTG system are listed below:

- <u>Availability of developed hardware and unit cost</u>. The hardware should be available within the anticipated launch date, with a high degree of confidence.

- <u>Nuclear Safety</u>. The RTG system should have a flight-qualified heat source available, or a design based on technology that will insure the availability of the final product.

- <u>Design Status</u>. It is desirable to have an RTG system that has been built, tested, and flown. However, a system composed of off-the-shelf components based on established technology would also be a good candidate. The existing system should have sufficient flexibility and growth potential to accommodate changes in mission requirements.

A summary of these criteria for each of the candidate RTG systems is shown in Table E-4.

Table E-4. Comparison of RTG Development and Availability

RTG System	Estimated Availability Date	Nuclear Status (Heat Source)	Design Status (Converter)	Configuration		Remarks
				Pioneer F/G	Pioneer Orbiter Baseline	
SNAP-19	1971	Proven	Completed satisfactorily	4 units	6-8 units	
HPG	1973	Proven	In-house prototype built and undergoing endurance test	2	4	SNAP-19 modification readily adaptable to Pioneer
MHW	1974	New design	Baseline design not established. New SiGe composition and high temperature insulation require characterization	1	2	Single unit unsuitable for spinning spacecraft

The summary shows that the Pioneer SNAP-19 and SNAP-19 HPG RTG's have the best potential for an early launch date since they are available today and hardware already exists. Selecting the SNAP-19 RTG would be undesirable since it is comparatively inefficient and would require six to

eight units which poses problems in mounting and deployment. The HPG and MHW will have a high power output which will allow a reduction in the number of RTG's used and a contingency factor for degradation.

4.2 RTG System Costs

Estimated costs for each candidate system are shown in Table E-5. Values are recurrent hardware costs for a single unit. They include hardware development and unit acceptance testing but no program management, administrative or qualification testing. The price of each unit assumes a fueled capsule (fuel plus capsule materials plus encapsulation) of the required size will be provided GFE by the AEC.

Table E-5. Candidate RTG System Cost

RTG System	Power (Watts)	Unit Cost ($K)	Remarks
Pioneer SNAP-19	40	130	Cost estimated by Isotopes, Inc. based on actual SNAP-19 Pioneer hardware costs include heat shield components. Unit costs reimbursible to the AEC for Pioneer G mission have been estimated to be no more than $750K each including fuel.
SNAP-19 HPG	65	225	Cost estimated by Isotopes, Inc. based on SNAP-19 Pioneer hardware costs. Increased costs result from higher priced components and fabrication costs.
MHW	159	400	Cost based on utilization of expensive components, materials of construction and new design techniques. For example, design uses complicated thermoelectric, multifoil insulation, and has beryllium radiator.

4.3 Spacecraft Integration

The requirements for convertibility from the present Pioneer F/G design to each candidate system are discussed below. Integration problems relative to the mechanical, thermal, electrical, and nuclear radiation interface are described.

Electrical Interface. Predictions of the time-dependent power degradation is plotted in Figure E-5 for the three candidate systems. The enhanced performance of the HPG system over the near- and long-term is predicated on improved thermoelectrics now under development.

The available power at the beginning and end of the orbital mission phase (2.5 and 3.5 years for the Jupiter orbiter, 5 and 6 years for the Saturn orbiter) projected for each of the candidate power sources is given in Table E-6. The number of RTG units envisioned is indicated in parentheses.
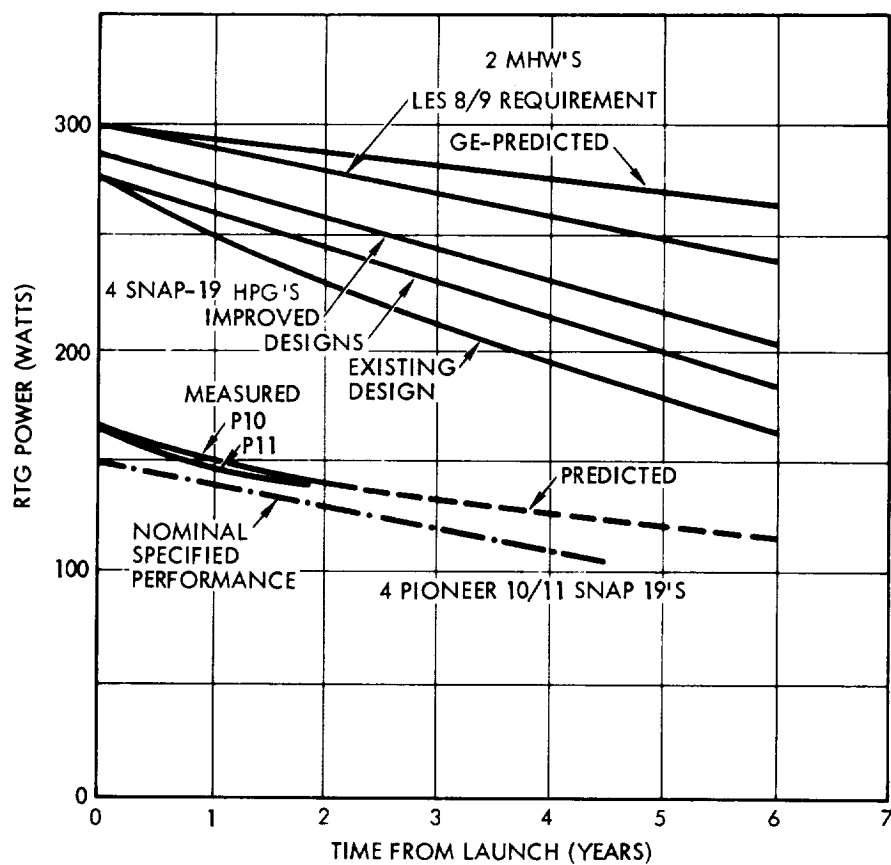
Figure E-5. Candidate RTG Performance Predictions

Table E-6. Projected Performance of Candidate RTG Systems (in watts)

RTG System	Jupiter Orbiter			Saturn Orbiter		
	Steady Loads*	Projected RTG Power at		Steady Loads*	Projected RTG Power at	
		Start Orbital	End Phase		Start Orbital	End Phase
SNAP-19 (6)	236.5	210	200	211.3	185	176
HPG (4)		250	238		218	204
MHW (2)		286	280		270	263

*Based on data in Table 3-5 (Section 3.4)

These data indicate that only the MHW system provides an adequate power margin (50 to 60 watts for the Jupiter and Saturn orbiter mission) to handle the steady loads of all subsystems, experiments and excess power contingencies. The system also has the advantage of operating at 28 volts which makes power conditioning simpler and more efficient.

The HPG system is relatively attractive since it operates at higher load voltage than the Pioneer SNAP-19 RTG's and since its design is based on the current technology used in the Pioneer 10 and 11 missions. However, it provides almost no power margin.

Mechanical and Structural Interface. The primary aspect of this interface is to minimize the impact on the basic spacecraft structure and mass properties, stay within the acceptable weight specification, and fit into the available volume.

A comparison of weights and volumes for each system is presented in Table E-7.

Table E-7. Weights and Volumes of Candidate RTG Systems

RTG	Weight Per Side (Pounds)	Weight Total (Pounds)	Volume Description* (Inches)
SNAP-19			
Two RTG's/side	60	120	16 x 22
Three RTG's/side	90	180	16 x 33
Four RTG's/side	120	240	16 x 44
HPG			
One RTG/side	38	76	24 x 13.5
Two RTG's/side	76	152	24 x 27.0
MHW			
One RTG	85	85	15.5 x 23
One RTG/side	85	170	15.5 x 23

*Diameter times length/side assuming tandem mounting.

The weight and volume of each system are reported per deployable mass on each side of the spacecraft. Since the spacecraft is spin-stabilized it is desirable to deploy the RTG's on opposite sides in order to maintain the deployed center-of-gravity along the spin axis. This can

be accomplished by mounting a counterweight to the extremity of the magnetometer boom which, when extended, will nullify the effect of the asymmetrical RTG deployment.

A comparison of the available space under the shroud with the volume of the deployable RTG's shows that all the candidate systems should fit within the envelope dimensions.

The RTG system selected should be capable of sustaining the qualification levels for acceleration, vibration, and shock representative of the Pioneer orbiter at launch. The Pioneer SNAP-19 is designed to sustain these qualification levels and therefore the HPG will probably sustain these loads. However, the MHW has not been designed for these values and analyses of the potential problems involved and redesign of the RTG's would probably be required to qualify this system.

The method of mounting each of the RTG's is similar. The mounting interface is at the cylindrical end of the RTG. Each RTG must be cantilevered individually at this point from supporting structure that adapts to the spacecraft. A bolted flange is used on all the generators.

The RTG systems that would be easiest to mount on advanced spacecraft are those systems requiring fewer units. Moreover, the electrical connections, cable mounting, and blockage of the RTG heat rejection system will be minimized. The use of six to eight SNAP-19 RTG's would be the most difficult systems to mount and install in the spacecraft.

Thermal Interfaces. The thermal interfaces requiring special attention are:

- Blockage of the RTG heat rejection system by the spacecraft and its components

- Heating of the spacecraft and its components during on-stand and during launch

- High temperatures during launch and prior to deployment.

The interference by the spacecraft in orbit can be minimized by deploying the RTG away from the spacecraft. However, during on-stand conditions when the RTG's are in the stowed position there may be critical areas requiring special insulation. On Pioneer 10/11 it was determined that heating effects in the stowed position and during launch were more critical on the high-gain antenna and side panels of the spacecraft. The side panel insulation was modified on the spacecraft and thermal insulators were incorporated in the RTG support structure to reduce the heat leakage into the spacecraft compartment. The antenna was also coated to reduce localized heating effects. In addition, air conditioning ducts to direct air flow are used on-stand to carry away the heat generated by the RTG's. The air conditioning will minimize local heat effects on the spacecraft and prevent RTG over-temperature during the launch phase.

The degree to which internal heat generation is a problem is determined primarily by the RTG fuel loading and the heat rejection temperatures. A summary of these characteristics for each of the generators is shown in Table E-8. It can be seen from the data in the table that in general PbTe RTG's (SNAP-19 and HPG) pose fewer problems because of their lower temperatures. The thermal interactions would be particularly important on configurations where a minimum change to the design is required. The use of a SiGe system (MHW) may require directed air flow or gaseous nitrogen to carry away the heat energy and to reduce the RTG surface temperature. In call cases the air conditioning load for higher power configurations will be considerably increased over the present Pioneer 10/11. This may necessitate an expansion of the on-stand air conditioning capability.

Table E-8. Thermal Characteristics of Candidate RTG Systems

RTG	Thermal Loading ($\sim$ Watts)	RTG Surface Temperature	
		In-Space (°F)	In-Air* (°F)
SNAP-19 (4)	2,580	300	240
HPG			
65 watt (2)	2,050	330	240
MHW (1)	2,200	590	536

*Based on natural convection heat transfer coefficients. Temperature can be reduced by using directed air flow or gaseous nitrogen in launch vehicle fairing.

Nuclear Radiation Interface. The SNAP-19 RTG's on the present Pioneer 10/11 contain approximately 2600 thermal watts of isotope fuel. The radiation produced by the radioisotope consists of high-energy neutrons ($\sim$2 MeV) and gammas (2.6 MeV and 0.8 MeV). The effects of this radiation on spacecraft using RTG's are displacement (integrated) damage to components and materials and interference (noise) with the science experiments. Neutrons are primarily responsible for integrated damage, whereas the gamma radiation may cause ionization in the sensitive science detectors thereby generating noise. The neutron fluence on Pioneer 10/11 was shown to be relatively small compared to the ionizing dosage from Jovian electrons and protons. The total ionizing dosage from these electrons and protons was 36,000 rads compared to approximately two rads dosage from the RTG's. The maximum fuel loading for any of the generators under consideration is at the most double that of the present Pioneer SNAP-19 units; therefore there does not appear to be a problem relative to displacement damage from RTG's for these missions.

Interference with science also does not appear to be a major problem. For advanced missions the maximum increase in radiation flux would be approximately double that of Pioneer 10/11. In Pioneer 10/11 one instrument avoided measurements in the 10-100 KeV range; another employed a small amount of shielding against gamma radiation. Otherwise, no significant interference was detected from the RTG's. Doubling the isotope thermal power would have a noticeable effect in this area, but it would not impose a significant penalty on instrument operation, assuming the same class of instruments is employed.